Effect of hydrodynamic dispersion on spherical reaction front dynamics in porous media

Pratyaksh Karan [1,*] Uddipta Ghosh [1,†] Fabian Brau,[2,‡]
Yves Méheust,[3,§] and Tanguy Le Borgne[3,‖]

[1]*Department of Mechanical Engineering, Indian Institute of Technology Gandhinagar,
Palaj, Gandhinagar, Gujarat 382055, India*
[2]*Université libre de Bruxelles (ULB), Nonlinear Physical Chemistry Unit,
Faculté des Sciences, CP231, 1050 Brussels, Belgium*
[3]*Université de Rennes 1, CNRS, Géosciences Rennes UMR 6118, Rennes 35042, France*

Reaction fronts sustained by fluid mixing play a central role in a large range of porous media systems and applications. In many cases, pointwise continuous injection of a reactant that displaces a resident reactant in three dimensions leads to a growing spherical reaction front. While such configurations have until now been studied under the assumption of a constant diffusion coefficient, in porous media the dominant diffusive process at the continuum scale is hydrodynamic dispersion, which depends linearly on the flow velocity. Here we analyze the impact of this nonuniform and time-varying hydrodynamic dispersion on reactive transport occurring in such a spherically advected reaction front under point injection and at constant flow rate. During an initial transient regime, dispersion leads to a more advanced reaction front and a larger global reaction rate than when molecular diffusion is the only mixing process, as well as to different temporal scalings for the reaction front properties. At larger times, the reaction front eventually reaches a steady state, characterized by a static position and time-independent reactant concentrations and reaction rate, regardless of the presence and strength of dispersion. When dispersion is weak, the steady-state front is positioned in a region where dispersion is negligible compared to diffusion. Conversely, when dispersion is large, the steady-state front is positioned in the transition zone where dispersion and diffusion are comparable. Under this condition, hydrodynamic dispersion permanently affects the reaction front's transport by altering the steady state itself and augmenting the global reaction rate.

I. INTRODUCTION

Reactive fronts, characterized as the region in which two miscible fluids, one of which displaces the other one, react with each other, are ubiquitous in natural and man-made porous media [1–3]. Such mixing fronts between chemically contrasted fluids have important applications in processes such as soil and aquifer remediation [4–6], CO_2 sequestration [7,8], hydrogen storage [9,10], geothermal systems [11], and the dynamics of subsurface microbial communities [12]. Reactive fronts in porous media also find presence in biological systems such as the extracellular matrix

_____

*pratyakshkaran@gmail.com

†uddipta.ghosh@iitgn.ac.in

‡fabian.brau@ulb.be

§yves.meheust@univ-rennes1.fr

‖tanguy.le-borgne@univ-rennes1.fr

(ECM) and affect cancer metastasis, disease propagation, and drug administration, to underline a few [13]. In the presence of imposed heterogeneous flows, such mixing fronts undergo continuous stretching and deformation [14–23], which enhance the effective mixing and reaction rates [24–26].

Mixing-induced reaction fronts are generally conceptualized as initially separated chemical species A and B, carried by miscible fluids, that react with each other when these fluids are mixed, following the bimolecular reaction $A + B \rightarrow C$ [27–34]. Among various possible flow scenarios, planar fronts subjected to linear stretching (simple shear) [25,35,36] and radially [27,28] and spherically [37] outward-moving fronts have received specific attention for their practical relevance. Spherical reaction fronts, generated from pointlike injection, exhibit nontrivial physical characteristics as they become stationary after a certain time, thus leading to steady-state spatial distributions of the reactant concentrations [37]. These nonuniform flow scenarios have so far been studied under the assumption of uniform diffusion coefficient.

In the context of transport in porous media (and in particular in subsurface hydrology), the Darcy scale is the smallest scale at which an upscaled (or volume-averaged) continuum description of flow and transport is applicable. Darcy scale modeling often provides valuable physical insights into the macroscopic transport processes without explicitly requiring a pore-scale description, which is computationally very expensive and generally even prohibitive [1,38]. In the corresponding mathematical description of solute transport, hydrodynamic dispersion is the Darcy scale manifestation of the interaction between molecular diffusion and advection by the heterogeneous pore scale velocity field. The resulting dispersion coefficient is expressed by a second rank tensor that is customarily taken to be a linear function of the local flow velocity [39–41]. In most practical cases, it dominates pure molecular diffusion by several orders of magnitude. Due to its dependence on the local Darcy velocity, hydrodynamic dispersion may strongly influence the dynamics of reactive fronts and thus significantly alter the local and global reaction rates [42,43]. However, its effect on spherical reaction fronts is so far unknown.

In the present study, we thus quantify the impact of dispersion on a spherical bimolecular reaction front, moving radially outward from a central injection point inside a porous medium. We develop a mathematical framework coupling the advection-dispersion-reaction equation (ADRE) and an irreversible bimolecular $A + B \rightarrow C$ reaction, the reactant A being continually injected at a point into a porous medium that is initially saturated with the species B. To isolate impact of hydrodynamic dispersion on the reaction front's dynamics, the medium's permeability here is assumed to be uniform. Heterogeneous permeability fields yield additional stretching of mixing fronts [44,45], which would otherwise combine with the mechanisms resulting from hydrodynamic dispersion. We carry out numerical simulations and derive asymptotic analytical solutions, which show good agreement with the numerical results. At early and intermediate times, hydrodynamic dispersion qualitatively alters the transient front properties (front location, width, and global reaction rate), while at sufficiently large times, the reaction front reaches a steady state. We further establish that in order for dispersion to have a permanent impact on the steady-state reaction's effective kinetics, its strength has to be above a critical threshold, which depends on the flow characteristics.

The rest of the article is arranged as follows. In Sec. II we describe the physical system and specify the notations, the governing equations along with the dispersion tensor's expression, and the relevant boundary conditions. We also briefly summarize the numerical solution methodology in this section. In Sec. III we derive the approximate analytical (asymptotic) solutions to the governing equations, present and discuss the numerical solutions, and compare the two. Finally, in Sec. IV we conclude and highlight the key findings and inferences.

II. THE GOVERNING EQUATIONS FOR REACTIVE TRANSPORT

A. Physical description of the spherically advected reaction front

We consider a homogeneous porous medium of uniform hydraulic conductivity K and uniform porosity ϕ_0, initially saturated by an ambient fluid containing a dissolved species B of uniform
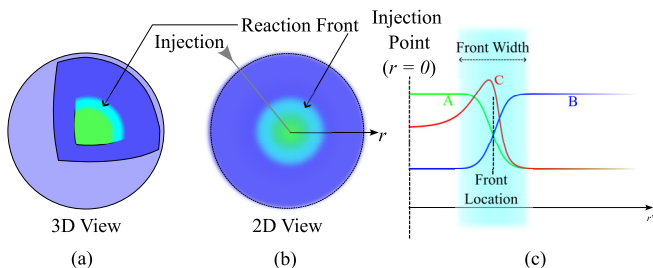
FIG. 1. Illustrative representations of the reaction front; the cartoon in (c) demonstrates a typical reaction front and the typical radial concentration profiles for the reactants (A and B) and the product (C) in the front's vicinity.

initial concentration (c_0). A second body of the same fluid, containing another dissolved species A of initially uniform concentration (also c_0), is being injected continuously from a central point into the porous medium with a permanent volumetric flow rate $4\pi Q_0$. As a result, the fluid containing species A invades the porous medium initially saturated by B, while A and B react at the interface between the injected and the resident fluids to produce C, as depicted in Fig. 1. Because of the uniform permeability (which results in a uniform hydraulic conductivity) of the porous medium and the spherical symmetry of the injection, the front will always have a spherical shape as it moves outward [see in Fig. 1(a)]. Porous domains with variable permeability would exhibit nonuniform stretching and deformation of the front [44,45]; the impact of such permeability heterogeneities on the reaction kinetics may be quantified in a subsequent study. We consider a first-order reaction kinetics in both the reactants (A and B), $R'(\mathbf{x}', t') = k_R c'_A(\mathbf{x}', t') c'_B(\mathbf{x}', t')$, where $R'(\mathbf{x}', t')$ is the local rate of reaction, $c'_i(\mathbf{x}', t')$ is the Darcy scale (averaged) concentration of species i (could indicate A, B, or C) at position $\mathbf{x}'$ and time t', and k_R is the reaction rate constant.

B. The hydrodynamic dispersion tensor

Hydrodynamic dispersion is the Darcy scale description of the spreading (mechanical as well as diffusive) of solutes at the Darcy scale, driven by pore-scale variability in the velocity and concentration. While for flow through confined open flow domains with small aspect ratios (such as tubes, or the space between parallel plates) Taylor dispersion is observed [46], for flows in porous media, dispersion is dominated by incomplete mixing, and neighboring streamlines may divert transversally from each other in a significant manner, which causes the mechanical dispersion coefficients (either longitudinal or transverse with respect to the local Darcy scale velocity) to vary linearly with the local velocity [1,38,47]. As such, the hydrodynamic dispersion tensor is expressed as (a concise reasoning for the choice of the dispersion tensor has been included in Appendix A)

$$\mathbf{D}^* = \mathbf{D}^*_M + \ell_T \|\mathbf{v}'\| \mathbf{I} + (\ell_L - \ell_T) \frac{\mathbf{v}' \mathbf{v}'^T}{\|\mathbf{v}'\|}, \tag{1}$$

where $\mathbf{D}^*_M$ is the effective molecular diffusion coefficient of the solute in porous media assumed to be $D_M \mathbf{I}$ (i.e., isotropic diffusivity), $\mathbf{v}'$ is the interstitial velocity (i.e., local fluid velocity averaged over the pore space), $\mathbf{I}$ is the identity tensor, and ℓ_T and ℓ_L are, respectively, the transverse and longitudinal mechanical dispersivities, which depend on the underlying geometrical features at the pore scale as well as the medium's porosity [1,38,47]. These lengths characterize the pore-scale heterogeneity of the medium, and in particular its impact on solute transport at the Darcy scale. More specifically, the isotropic part of $\mathbf{D}^*$ is associated with the mechanical as well as diffusive spreading of the solute along the direction of the macroscopic (Darcy scale) concentration gradient, whereas the nonisotropic part [i.e., the last term of Eq. (1)] quantifies the rate of spreading in the direction transverse to it. For the radial flow scenario studied here, the transverse dispersivity does not play

TABLE I. Characteristic scales of relevant variables.

Variable	Characteristic scale	Remarks
Concentration (c_c)	c_0	Injection concentration of species A (same as ambient concentration of B)
Time (t_c)	$(k_R c_0)^{-1}$	Reaction timescale
Coordinate length (r_c)	$[(Q_0/\phi_0)/(k_R c_0)]^{1/3}$	Volume flow rate is $4\pi Q_0$
Velocity (v_c)	$(Q_0/\phi_0)/r_c^2$	
Hydraulic head (h_c)	$Q_0/K r_c$	

a role, so that the dispersion tensor simplifies to $(\ell_L \|\mathbf{v}'\| + D_M)\mathbf{I}$, which is linearly dependent on the velocity magnitude $\|\mathbf{v}'\|$ and the molecular diffusivity D_M. If one disregards hydrodynamic dispersion ($\ell_L = \ell_T = 0$), the dispersion tensor simply reduces to the isotropic molecular diffusion tensor. Furthermore, in flow geometries with point injection, such as the one investigated here, ℓ_T is irrelevant as the symmetry of the system nullifies any nonradial solute transport.

C. Governing equations for the concentrations of A, B, and C

Flow in the porous medium is governed by Darcy's law, while the dynamics of chemical species concentrations are governed by the advection-dispersion-reaction equation (ADRE). Since these equations are well established, we directly consider their dimensionless versions (denoted without the prime). To this end, the dimensionless version of any variable, say, ψ' (which could represent c_A', $\mathbf{x}'$, t', etc.) is written as $\psi = \psi'/\psi_c$, where ψ_c is the characteristic scale of the said variable. Characteristic scales for all the pertinent variables are listed in Table I.

Note that here the only naturally occurring timescale is the typical reaction timescale, which has been chosen as $t_c = 1/(k_R c_0)$. The other two well-defined quantities are, respectively, the volumetric flow rate ($4\pi Q_0$) and the reactant concentration (c_0). These variables (along with the reaction rate constant, k_R) are sufficient to define the characteristic scales for length, velocity, etc., as shown in Table I. Note that the length scale has been chosen as the distance that a fluid particle, moving at the characteristic velocity v_c, travels during the characteristic reaction time. In the following, we shall use the spherical polar coordinates for mathematical modeling. As such, because of the axisymmetric nature of the problem, all concentrations will be functions of r and t only.

After enforcing the nondimensionalization scheme mentioned above, the fluid mass conservation with the discharge rate expressed as a function of the hydraulic head's gradient according to Darcy's law reads $(1/r^2)\partial/\partial r(-r^2 K \partial h/\partial r) = 0$, where h is the hydraulic head and yields for the interstitial velocity (the interstitial velocity is the discharge rate divided by the porosity),

$$\mathbf{v} = v_r \hat{\mathbf{e}}_r = \frac{1}{r^2}\hat{\mathbf{e}}_r, \tag{2}$$

which is purely radial. With the help of Eq. (1), and assuming that the molecular diffusivities of all chemical species are identical, the ADRE may be generally written for the species i as [1,25,26,38]

$$\frac{\partial c_i}{\partial t} + v_r \frac{\partial c_i}{\partial r} = \frac{1}{\text{Pe}}(\eta \text{Pe}\, v_r + 1)\frac{1}{r^2}\frac{\partial}{\partial r}\left(r^2 \frac{\partial c_i}{\partial r}\right) + \eta \frac{\partial v_r}{\partial r}\frac{\partial c_i}{\partial r} + R_i(r,t), \tag{3a}$$

$$\text{with } R_i(r,t) = \begin{cases} -c_A c_B & \text{when } i = \text{A, B} \\ +c_A c_B & \text{when } i = \text{C} \end{cases}. \tag{3b}$$

A concise derivation of the above equation has been provided in Appendix B.

Two crucial dimensionless numbers appear in the above equation. These are (1) the Péclet number Pe, which characterizes the ratio of the diffusion timescale to the advection timescale and

has the expression [38]

$$\text{Pe} = \frac{r_c^2/D_M}{r_c/v_c} = \frac{(Q_0/\phi_0)}{r_c D_M}, \tag{4}$$

where D_M is the species' molecular diffusivity, and (2) η, defined as the dimensionless longitudinal dispersivity, which essentially characterizes the strength of mechanical dispersion; it is expressed as

$$\eta = \frac{\ell_L}{r_c}. \tag{5}$$

By extension, ηPe is the typical ratio of mechanical dispersion to molecular diffusion. Usually, the ADREs also entail the Damköhler number (Da) [38], defined as the ratio of the typical diffusion timescale (t_D) to the typical reaction timescale (t_r) such that $\text{Da}/\text{Pe} = t_a/t_r$, where $t_a = r_c/v_c$ is the advection timescale. Since in the present configuration $t_a = 1/(k_R c_0) = t_r$, one naturally ends up with $\text{Da} = \text{Pe}$. Therefore, the relative importance of reaction (characterized by R_i) and diffusion in Eq. (3a) is also characterized by the Péclet number.

Equation (3a) is subject to the boundary conditions $c_A = 1$, $c_B = \partial c_C/\partial r = 0$ as $r \to 0$ and $c_B = 1$, $c_A = \partial c_C/\partial r = 0$ as $r \to \infty$, as well as the initial condition $c_B = 1$, $c_A = c_C = 0$ at $t = 0, \forall\, r$.

We may substitute the expression for v_r from Eq. (2) in Eq. (3), which then simplifies to

$$\text{Pe}\frac{\partial c_i}{\partial t} = \left(\frac{\eta\text{Pe}}{r^2} + 1\right)\frac{\partial^2 c_i}{\partial r^2} + \left(\frac{2r - \text{Pe}}{r^2}\right)\frac{\partial c_i}{\partial r} + \text{Pe}\, R_i. \tag{6}$$

III. RESULTS AND DISCUSSION

Equation (6) is solved numerically using an implicit finite difference scheme, along with source term linearization to handle the nonlinear reaction terms. Further details on the numerical scheme are given in Appendix C. In the following, approximate analytical solutions will also be discussed.

We use these numerical and approximate analytical solutions to quantify the impact of dispersion, which corresponds to finite values of η, on the front's propagation and reaction rates. The dispersion-free scenario corresponding to $\eta = 0$ has been previously explored by Comolli *et al.* [37]. As expected, our solutions for the limiting case $\eta = 0$ agree with the ones reported by these authors. In Sec. III A we shall first summarize some of the key properties of the front, and in Sec. III B we shall simultaneously present our inferences from the analytical and the numerical solutions.

We have also explored (numerically) the scenarios where the reactants have distinct initial concentrations, and found that the essential physics in such cases remains similar to that of identical initial reactant concentrations (c_0) considered in the present analyses. In particular, the scaling insights and the analytical approximations discussed ahead do remain applicable to reactive transport processes where the initial concentrations of A and B are different, as verified by the numerical solutions of Eq. (6). Hence, in order to delineate the consequences of dispersion in a focused manner, the results of scenarios with distinct initial concentrations of the reactants are not presented in the following. Note also that the consequences of different initial concentrations of the reactants have previously been explored by Comolli *et al.* [37] in a dispersion-free context.

A. Observables characterizing the reaction front

While Eq. (6) governs the transport of the dissolved species, it is nonlinear owing to the presence of the reaction term $\text{Pe}R_i$, and thus it is difficult to extract analytical insights from this equation. However, by defining a new variable $\theta = c_A - c_B$, it becomes possible to track the front location, since $\theta \ll 1$ close to the front where both the reactants are present in significant amount, while $\theta \approx \pm 1$ away from the front. At the same time, a linear governing equation for θ may be derived by

subtracting (6) for c_B from c_A, and this yields

$$\text{Pe}\frac{\partial \theta}{\partial t} = \left(\frac{\eta\text{Pe}}{r^2} + 1\right)\frac{\partial^2 \theta}{\partial r^2} + \left(\frac{2r - \text{Pe}}{r^2}\right)\frac{\partial \theta}{\partial r}, \tag{7}$$

subject to boundary conditions: $\theta(r = 0, t > 0) = 1$ and $\theta(r \to \infty, t > 0) \to -1$, and to initial conditions: $\theta(r = 0, t = 0) = 1$ and $\theta(r \neq 0, t = 0) = -1$. Equation (7) is evidently a conservative equation for θ which quantifies the difference in the local reactant concentrations. In what follows, we shall first discuss the nature of the transient solutions to the above equation using analytical approximations, while later it will be shown that Eq. (7) also admits a stationary solution. However, it is first important to outline some general front properties, whose analytical approximations (along with numerical solutions) will be reported in the later sections.

First, the reaction front location r_f may be defined as the location where $\theta = 0$ (or $c_A = c_B$) [32]. The reaction rate is expected to be large at this location where both c_A and c_B are present in significant quantity, as it demarcates the boundary where the dominant reactant concentration switches from c_A to c_B. Second, the reaction front half-width w_f (denoted simply as "width" henceforth for the sake of brevity), quantifying the thickness of the region where an appreciable rate of reaction is observed, may be mathematically linked to the normalized second moment of the reaction rate about the reaction front, as follows [32]:

$$w_f = \left[\frac{\int_0^\infty 4\pi r^2 c_A c_B (r - r_f)^2 \, dr}{\int_0^\infty 4\pi r^2 c_A c_B \, dr}\right]^{\frac{1}{2}}. \tag{8}$$

Third, the normalized global reaction rate $\bar{R}$ may be evaluated by integrating the local reaction rate ($R = c_A c_B$) over the entire domain:

$$\bar{R}(t) = 4\pi \int_0^\infty c_A c_B \, r^2 \, dr. \tag{9}$$

However, we emphasize that the local reaction rate has an appreciable magnitude only within the reaction front; therefore, the global reaction rate $\bar{R}$ is also a front property. Finally, the mass of the product may be computed as

$$M_C(t) = 4\pi \int_0^\infty c_C \, r^2 dr. \tag{10}$$

However, integrating Eq. (6) for c_C, we observe that M_C is alternatively also expected to be given by the integral

$$M_C(t) = \int_0^t dt^* \bar{R}(t^*). \tag{11}$$

B. Behavior of the spherical reaction front

In Eq. (7) the term $(\eta\text{Pe}/r^2 + 1)$ represents both mechanical dispersion and molecular diffusion, wherein the component $\eta\text{Pe}/r^2$ (here $1/r^2$ is just the local velocity) quantifies the strength of mechanical dispersion. When this component is much larger than unity, mechanical dispersion dominates over molecular diffusion and $(\eta\text{Pe}/r^2 + 1)$ may be approximated as $\eta\text{Pe}/r^2$. This occurs in the vicinity of the reaction front if the front location satisfies $r_f^2 \ll \eta\text{Pe}$. Conversely, molecular diffusion takes over when $r_f^2 \gg \eta\text{Pe}$; this is due to the radial $1/r^2$ decrease of the flow velocity. As a result, it is expected that at early times (when $t \ll 1$) the front's spreading will be dominated by mechanical dispersion. On the other hand, at longer times ($t \gg 1$), the front may enter a nondispersive regime, where diffusive transport is dominated by molecular diffusion rather than mechanical dispersion. This second regime is realized only when the front progresses for a sufficiently long time before reaching a stationary state, where $\partial\theta/\partial t = 0$. Indeed, as previously shown by Comolli

et al. [37] (for the special case of $\eta = 0$) and as we shall establish later, a spherically advected front will always reach a steady state, provided it is allowed to travel for a sufficiently long time. When mechanical dispersion is sufficiently strong (quantified as $\eta \gg$ Pe), we establish that the front may become static at a location where dispersion is comparable to diffusion, and hence the nondispersive regime mentioned earlier never materializes. In addition to this, here we shall depict that for ηPe $\gg 1$, i.e., when diffusion is weak (Pe $\gg 1$, provided η is not too small) and/or dispersion is strong ($\eta \gg$ Pe, provided Pe is not too small), the front may further go through another intermediate mixing-limited regime at moderately large times ($t \gg 1$), wherein the reaction rate as well as the front width decays with time before reaching the aforementioned steady state.

1. The early-time (t ≪ 1) behavior: Dispersion-dominated reaction-limited regime

At early times, the reaction front is sufficiently close to the injection point and occupies a sufficiently small region for the following two statements to hold within the reaction zone: (1) $r^2 \ll \eta$Pe and (2) $|\eta$Pe $\partial^2\theta/\partial r^2| \gg |(2r -$ Pe$)\partial\theta/\partial r|$. The second condition stems from the fact that within the reaction front, $\partial^2\theta/\partial r^2 \sim 1/w_f^2$ (w_f being the front width) and $\partial\theta/\partial r \sim 1/w_f$, with $w_f \ll 1$ at early times. As a consequence, keeping only the dominant terms along with a change of variable $\tilde{r} = r/\eta^{1/4}$ simplifies Eq. (7) to

$$\frac{\partial\theta}{\partial t} = \frac{1}{\tilde{r}^2}\frac{\partial^2\theta}{\partial\tilde{r}^2}. \tag{12}$$

Subsequently, the above equation may be transformed into an ODE using the similarity variable $\xi = \tilde{r}^4/t$. With this similarity variable, the term $\partial\theta/\partial t$ transforms into $-(\xi/t)d\theta/d\xi$ and the term $(1/\tilde{r}^2)\partial^2\theta/\partial\tilde{r}^2$ transforms into $(16\xi^2 d^2\theta/d\xi^2 + 12\xi d\theta/d\xi)/(\xi t)$, such that Eq. (12) transforms into the ODE:

$$\frac{d^2\theta}{d\xi^2} + \frac{12 + \xi}{16\xi}\frac{d\theta}{d\xi} = 0. \tag{13}$$

Using the boundary conditions $\theta(0) = 1$ and $\theta(\infty) = -1$, the solution to Eq. (13) is

$$\theta(\xi) = -1 + 2\bar{\Gamma}\left(\frac{1}{4}, \frac{\xi}{16}\right), \tag{14}$$

where $\bar{\Gamma}(a, x)$ is the regularized gamma function [48], which is the ratio of the incomplete gamma function $\Gamma(a, x)$ and the complete gamma function $\Gamma(a)$. At the front location, $\theta = 0$, which gives the expression for r_f as

$$r_f = \left[16\bar{\Gamma}^{-1}\left(\tfrac{1}{4}, \tfrac{1}{2}\right)\right]^{\frac{1}{4}}\eta^{\frac{1}{4}}t^{\frac{1}{4}} = 0.914\eta^{\frac{1}{4}}t^{\frac{1}{4}}. \tag{15}$$

Thus, the front location should scale as $r_f \sim t^{1/4}$ at early times, which shows a qualitative departure from the nondispersive transport characterized by $r_f \sim t^{1/3}$ [37] (also see Appendix E for a concise derivation). This indicates that the front moves at approximately the same rate as a fluid parcel ($\sim t^{1/3}$) when dispersion is absent, whereas the presence of dispersion quantitatively changes its rate of advancement. This is a direct consequence of the large enhancement in the spreading of the reactants due to dispersion at early times ($t \to 0$) near the injection point, where the flow velocity is large ($r_f \ll 1$), thus amplifying the influence of mechanical dispersion in the process. The dominance of mechanical dispersion at early times because of large radial velocities also becomes clear from Eq. (12), and this gives rise to a dispersion-dominated reaction-limited regime, because of limited progress in the overall reaction (since $t \ll 1$).

Now we assess the early-time ($t \ll 1$) behavior of the reaction front. Following a similar ansatz to those employed in previous dispersion-free ($\eta = 0$) studies [37], we consider c_A and c_B to be of the following form in the vicinity of the front:

$$c_A = G_A(z), \quad c_B = G_B(z), \quad z = \frac{r - r_f}{t^\alpha}, \tag{16}$$

where both G_A and G_B are functions of the similarity variable z only. Proceeding with this expression for c_A and c_B, with the objective of obtaining a similarity solution at early times, Eq. (6) for c_A as well as c_B in the vicinity of the reaction front transforms to

$$
\left[\frac{\eta \mathrm{Pe}}{\left(zt^{\alpha-\frac{1}{4}}+0.914\,\eta^{\frac{1}{4}}\right)^2}+t^{\frac{1}{2}}\right]\frac{d^2G_i}{dz^2}+\left[\frac{2t^{\alpha+\frac{1}{4}}}{\left(zt^{\alpha-\frac{1}{4}}+0.914\,\eta^{\frac{1}{4}}\right)}-\frac{\mathrm{Pe}t^\alpha}{\left(zt^{\alpha-\frac{1}{4}}+0.914\,\eta^{\frac{1}{4}}\right)^2}\right.
$$
$$
\left.+\alpha\mathrm{Pe}zt^{2\alpha-\frac{1}{2}}+\frac{0.914\,\eta^{\frac{1}{4}}\mathrm{Pe}}{4}t^{\alpha-\frac{1}{4}}\right]\frac{dG_i}{dz}-\mathrm{Pe}t^{2\alpha+\frac{1}{2}}G_AG_B=0,\quad i=A/B, \tag{17}
$$

where $r_f = 0.914\,\eta^{1/4}t^{1/4}$, based on Eq. (15). To assess the early-time regime, we consider Eq. (17) in the limit $t \to 0$ with z fixed. It may be shown that in this limit, a physically and mathematically consistent solution for c_A requires $\alpha = 1/4$ (see Appendix D 1), with which Eq. (17) simplifies to $d^2G_i/dz^2 + (4\eta)^{-1}(z + 0.914\,\eta^{1/4})^3 dG_i/dz = 0$, where $i \equiv A$ or B. Subsequently conducting a change of variables $z = \eta^{1/4}\tilde{z}$, we arrive at the equation

$$
\frac{d^2G_i}{d\tilde{z}^2} + \frac{(z+0.914)^3}{4}\frac{dG_i}{d\tilde{z}} = 0, \tag{18}
$$

which is subjected to the boundary conditions $G_A(\tilde{z} = -0.914) = 1$, $G_B(\tilde{z} = -0.914) = 0$, $G_A(\tilde{z} = \infty) = 0$, and $G_B(\tilde{z} = \infty) = 1$ (based upon the conditions for θ given after Eq. (7)). Evidently, this equation along with its boundary conditions is universal, i.e., independent of η (as well as Pe). Substituting the expression for r in terms of $\tilde{z}$ from Eq. (16), $r = t^{1/4}\eta^{1/4}(\tilde{z} + 0.914)$, into (9), we obtain

$$
\bar{R}(t) = I_0\eta^{\frac{3}{4}}t^{\frac{3}{4}} = 6.30\,\eta^{\frac{3}{4}}t^{\frac{3}{4}}. \tag{19}
$$

In the equation above, $I_0 = \int_{-0.914}^{\infty} G_A(\tilde{z})G_B(\tilde{z})(\tilde{z} + 0.914)^2\,d\tilde{z}$ is evaluated to the numerical constant 6.30 due to the universal nature of Eq. (18). Upon using Eq. (11), we may further deduce that the product mass should follow the expression

$$
M_C(t) = 3.60\,\eta^{\frac{3}{4}}t^{\frac{7}{4}}. \tag{20}
$$

Owing to the factor $\eta^{3/4}$ in Eq. (19), for sufficiently strong dispersion the instantaneous global reaction rate becomes larger than that in a dispersion-free scenario. This is because dispersion-driven spreading of the reactants leads to enhanced mixing at early times, which results in an augmented global reaction rate.

On the other hand, using Eq. (8), the width may be estimated as

$$
w_f = I_1\,\eta^{\frac{1}{4}}t^\alpha = 0.78\,\eta^{\frac{1}{4}}t^{\frac{1}{4}}, \tag{21}
$$

where $I_1 = \sqrt{(\int_{-c}^{\infty}(\tilde{z}+c)^2 G_A(\tilde{z})G_B(\tilde{z})\tilde{z}^2\,d\tilde{z})/(\int_{-c}^{\infty}(\tilde{z}+c)^2 G_A(\tilde{z})G_B(\tilde{z})\,d\tilde{z})}$ (with $c = 0.914$) is also a numerical constant equal to 0.78 owing to the universal nature of Eq. (18).

When $\eta = 0$, at early times the front exhibits diffusion-dominated reaction-limited behavior, in contrast to the dispersion-dominated behavior shown here. Approximate analytical estimates for the early-time front properties in the dispersion-free case (i.e., $\eta = 0$, previously reported by Comolli *et al.* [37]) are given in Appendix E. This regime may also be realized in the presence of dispersion, provided it is sufficiently weak, as we shall observe in Sec. III B 5 and Sec. III B 6.

2. The intermediate-time ($1 \ll t \ll t_{SS}$) behavior: Dispersion-dominated mixing-limited regime

For sufficiently large values of η and Pe, i.e., for sufficiently strong mechanical dispersion as compared to molecular diffusion, the numerical solutions suggest that (see Figs. 2 and 3) even at large times ($t \gg 1$), the following conditions are satisfied within the reaction front: (1) $r_f^2 \ll \eta\mathrm{Pe}$

(mechanical dispersion dominates) and (2) $|\eta \mathrm{Pe}\, \partial^2\theta/\partial r^2| \gg |(2r - \mathrm{Pe})\partial\theta/\partial r|$. As a consequence, the approximate solution for θ in the form $\theta = F(\xi)$ and the front advancement in the form $r_f \approx 0.914\, \eta^{1/4}t^{1/4}$ still remain valid when $t \gg 1$. It has to be noted that the front eventually reaches a stationary state when $t = t_{SS}$ (see Sec. III B 3 and III B 4 for a detailed discussion), and hence the time period under consideration must also satisfy $t \ll t_{SS}$.

Now, we assess the intermediate-time ($1 \ll t \ll t_{SS}$) behavior of the reaction front. In the vicinity of the front, θ may be approximated (using Taylor series expansion) as

$$\theta = -\mathcal{K}\frac{(r - r_f)}{t^{\frac{1}{4}}}, \quad \text{where} \quad \mathcal{K} = \frac{1.056}{\eta^{1/4}}. \tag{22}$$

Following a similar ansatz to those employed in previous dispersion-free ($\eta = 0$) studies [37], we consider c_A to be of the form

$$c_A = t^{-\frac{\beta}{2}}G(z), \quad z = \frac{r - r_f}{t^\alpha}. \tag{23}$$

Here the variable $G(z)$ quantifies the concentration profile of A and the factor $t^{-\frac{\beta}{2}}$ quantifies the depletion of A close to the reaction front. Proceeding with this expression for c_A, with the objective of obtaining similarity solutions for the intermediate-time regime, it may be shown (see the work of Gálfi and Rácz [32] for a detailed step-by-step argument) by considering the region behind the reaction front that, as $z \to -\infty$, $G(z)$ must satisfy $G \sim -z$, from which it follows that, $\alpha + \beta/2 - 1/4 = 0$.

Furthermore, substituting c_A from Eq. (23) into Eq. (6), using the approximate expression for θ from Eq. (22) and the relation $c_B = c_A - \theta$, Eq. (6) for c_A in the vicinity of the reaction front transforms into

$$\left[\frac{\eta \mathrm{Pe}\, t^{-\frac{1}{2}}}{\left(zt^{\alpha-\frac{1}{4}} + 0.914\, \eta^{1/4}\right)^2} + 1\right]\frac{d^2G}{dz^2} + \left[\frac{2t^{\alpha-\frac{1}{4}}}{\left(zt^{\alpha-\frac{1}{4}} + 0.914\, \eta^{1/4}\right)} - \frac{\mathrm{Pe}t^{\alpha-\frac{1}{2}}}{\left(zt^{\alpha-\frac{1}{4}} + 0.914\, \eta^{1/4}\right)^2}\right.$$

$$\left. + \alpha \mathrm{Pe}zt^{2\alpha-1} + \frac{0.914\, \eta^{1/4}\mathrm{Pe}}{4}t^{\alpha-3/4}\right]\frac{dG}{dz} - \mathrm{Pe}t^{3\alpha-\frac{1}{4}}(G^2 + \mathcal{K}zG) + \frac{\beta \mathrm{Pe}}{2}t^{2\alpha-1}G = 0. \tag{24}$$

It may be observed from the first bracketed term in the above equation that $|\eta \mathrm{Pe}\, t^{-1/2}/(zt^{\alpha-1/4} + 0.914\, \eta^{1/4})^2| \geqslant O(1)$ is possible even when $t \gg 1$, provided that

$$t \ll t_{SS}, \quad \eta \geqslant O(1) \quad \text{and} \quad \eta \mathrm{Pe}^2 \gg 1. \tag{25}$$

This is because for $\eta \geqslant O(1)$, the term $(\eta \mathrm{Pe}\, t^{-\frac{1}{2}})/(zt^{\alpha-\frac{1}{4}} + 0.914\, \eta^{1/4})^2$ may become larger than unity even for $t \gg 1$. This will occur when $\alpha < 1/4$, due to which $zt^{\alpha-1/4}$ will be negligible compared to $0.914\eta^{1/4}$ provided that $1 \ll t \ll \eta \mathrm{Pe}^2$. Consequently, when $\eta \mathrm{Pe}^2$ is sufficiently large, this condition may be satisfied even when $t \gg 1$. Therefore, with $\eta \mathrm{Pe}^2 \gg 1$ and thereby $\eta \mathrm{Pe}\, t^{-1/2}/(zt^{\alpha-1/4} + 0.914\, \eta^{1/4})^2$ retained in the leading order, it may further be shown that a physically consistent solution for c_A when $t \gg 1$ (provided $t \ll t_{SS}$) requires $\alpha = -1/12$ (see Appendix D 2 for a brief derivation), giving $\beta = 2/3$ (since $\alpha + \beta/2 - 1/4 = 0$). Equation (24) then simplifies to $d^2G/dz^2 + [(1.828t^{1/6})/(\eta^{3/4}\mathrm{Pe})]dG/dz - (0.835/\eta^{1/2})(G^2 + \mathcal{K}zG) = 0$. Furthermore, since $\eta \geqslant O(1)$, $t \ll \eta \mathrm{Pe}^2$ and $\eta \mathrm{Pe}^2 \gg 1$, the term $[(1.828t^{1/6})/(\eta^{3/4}\mathrm{Pe})]$ is small compared to the rest of the coefficients in the above equation, and therefore Eq. (24) further simplifies to $d^2G/dz^2 - (0.835/\eta^{1/2})(G^2 + \mathcal{K}zG) = 0$. With another change of variable $\tilde{z} = z/\eta^{1/4}$, this equation transforms into

$$\frac{d^2G}{d\tilde{z}^2} - 0.835(G^2 + 1.056\, \tilde{z}G) = 0 \tag{26}$$

TABLE II. Expected timescaling of front properties and mass of product based on the analytical approximations discussed in Sec. III B; t_{SS} is the time at which the reaction front reaches a steady state.

	Dispersion-dominated reaction-limited ($t \ll 1$, $r_f^2 \ll \eta \text{Pe}$)	Diffusion-dominated reaction-limited ($t \ll 1$, $r_f^2 \gg \eta \text{Pe}$)	Dispersion-dominated mixing-limited ($1 \ll t \ll t_{SS}$, $r_f^2 \ll \eta \text{Pe}$)
r_f	$t^{1/4}$	$t^{1/3}$	$t^{1/4}$
w_f	$t^{1/4}$	$t^{1/2}$	$t^{-1/12}$
$\bar{R} = \int_{r \to 0}^{r \to \infty} 4\pi r^2 c_A c_B \, dr$	$t^{3/4}$	$t^{7/6}$	$t^{-1/4}$
$M_C = \int_{r \to 0}^{r \to \infty} 4\pi r^2 c_C \, dr$	$t^{7/4}$	$t^{13/6}$	$t^{3/4}$

and is subjected to the boundary conditions: $G \to -1.056\tilde{z}$ as $\tilde{z} \to -\infty$ and $G \to 0$ as $\tilde{z} \to \infty$. We therefore have a universal equation for G as a function of $\tilde{z}$ in Eq. (26). Now, substituting the similarity expressions for c_A [Eq. (23)] and c_B [$= t^{-\beta/2}(G + 1.056\tilde{z})$] and the expression for $\tilde{z}$ in terms of t and r into Eq. (9), we may deduce that the global reaction rate follows the expression

$$\bar{R}(t) = 4\pi t^{-\beta+\alpha} \eta^{\frac{1}{4}} \int_{-r_f/(\eta^{\frac{1}{4}} t^\alpha)}^{\infty} G(\tilde{z})(G(\tilde{z}) + 1.056\tilde{z}) \left(r_f + \eta^{\frac{1}{4}} t^\alpha \tilde{z} \right)^2 d\tilde{z}, \quad (27)$$

where $\alpha = -1/12$ and $\beta = 2/3$. Considering that at $t \gg 1$, (1) $G(\tilde{z})(G(\tilde{z}) + 1.056\tilde{z})$ peaks around $\tilde{z} = 0$ so that $\tilde{z}$ does not become large in the vicinity of the reaction front, as well as (2) $r_f/(\eta^{\frac{1}{4}} t^\alpha) \sim t^{1/3} \gg 1$, we approximate $(r_f + \eta^{\frac{1}{4}} t^\alpha \tilde{z})^2 \approx r_f^2 = 0.835\eta^{1/2} t^{1/2}$. Then taking the lower limit of the integral in Eq. (27) as $-\infty$, it simplifies to

$$\bar{R}(t) = 13.27 \eta^{\frac{3}{4}} t^{-\frac{1}{4}}, \quad (28)$$

where we have utilized Eq. (26) to evaluate the integral $\int_{-\infty}^{\infty}(G^2 + 1.056\tilde{z}G)d\tilde{z}$ as $1.2[G']_{\tilde{z} \to -\infty}^{\tilde{z} \to \infty}$, which is equal to 1.26.

Upon using Eq. (11), we may further deduce that the product mass follows the expression

$$M_C(t) = 17.69 \, \eta^{\frac{3}{4}} t^{\frac{3}{4}}. \quad (29)$$

Following an approach similar to that for deriving $\bar{R}$ in Eq. (28), using Eq. (8), the width may be estimated as

$$w_f = 1.438 \, \eta^{\frac{1}{4}} t^{-\frac{1}{12}}. \quad (30)$$

The scaling expectations set forth above in Sec. III B 1 and Sec. III B 2, and in Appendix E, are summarized in Table II.

It may be observed that the presence of mechanical dispersion can qualitatively alter the transient behavior of the reaction front as compared to the dispersion-free scenario. Notice that during this intermediate regime, the global reaction rate actually decreases with time because the reactants are consumed at an accelerated rate during the early-time reaction-limited regime in the presence of dispersion, which causes them to get depleted near the front, thus leading to an overall drop in the reaction rate. This depletion of the reactants also causes the width of the front to shrink with time, as noted in Eq. (30). We thus conclude that the reaction rate during this time period is mainly dictated by how well the reactants have mixed, which turns it into a dispersion-dominated mixing-limited regime. Recall that at early times, the global reaction rate and the front width vary as $\bar{R} \sim t^{3/4}$ and $w_f \sim t^{1/4}$ [see Eqs. (19) and (21)], while in the current regime both decay with time, thus indicating that $\bar{R}$ (as well as the front width w_f) must go through a maximum at $t \sim O(1)$, when the condition (25) is satisfied. In contrast, without any mechanical dispersion, the global reaction rate would vary monotonically with time [37] towards the steady-state asymptote, hence culminating in a qualitatively different intermediate-time behavior. On the other hand, condition (25) clearly establishes that the mere presence of mechanical dispersion is not sufficient for the mixing-limited

regime to exist; it materializes only when $\eta \mathrm{Pe}^2$ is sufficiently large so that there is a large separation between $t = 1$ and t_{SS}. This requires molecular diffusion to be weak and mechanical dispersion to be stronger than a critical threshold, depending on the regime of dispersion.

In the dispersion-free scenario ($\eta = 0$) also, the mixing-limited regime may occur. In that case, the observed scalings are different from the dispersion-dominated scenario and exhibits [37]: $r_f \sim t^{1/3}$, $w_f \sim t^{1/6}$, $\bar{R} \sim t^{1/6}$, $M_C \sim t^{7/6}$. We indeed recover the same scalings from our numerical simulations in the dispersion-free system, as shown later in Sec. III B 5.

3. The steady-state solution

It may be shown that by setting $\partial \theta / \partial t = 0$ in Eq. (7), it is possible to derive a steady-state solution for $\theta(r)$, which has the following form:

$$\theta_{(S)} = 1 - 2 \left\{ \frac{1 - \exp\left[\sqrt{\frac{\mathrm{Pe}}{\eta}} \tan^{-1}\left(\frac{r}{\sqrt{\eta \mathrm{Pe}}}\right)\right]}{1 - \exp\left(\frac{\pi}{2}\sqrt{\frac{\mathrm{Pe}}{\eta}}\right)} \right\}, \tag{31}$$

where the subscript (S) denotes the "steady" state. The location where θ is zero is then defined as the static reaction front $r_{f(S)}$ and is given by

$$r_{f(S)} = \sqrt{\eta \mathrm{Pe}} \tan \left\{ \sqrt{\frac{\eta}{\mathrm{Pe}}} \ln \left[\frac{1}{2} + \frac{1}{2} \exp\left(\frac{\pi}{2}\sqrt{\frac{\mathrm{Pe}}{\eta}}\right) \right] \right\}. \tag{32}$$

In order to get an approximation for the steady-state global reaction rate $\bar{R}_{(S)}$, we consider the Taylor series expansion of $\theta_{(S)}$ [Eq. (31)] about $r_{f(S)}$,

$$\theta_{(S)} \simeq -K_S(r - r_{f(S)}), \quad \text{where} \tag{33a}$$

$$K_S = \frac{1}{\sqrt{\eta \mathrm{Pe}}} \cos^2 \left(\sqrt{\frac{\eta}{\mathrm{Pe}}} \ln \left\{ \frac{1}{2}\left[1 + \exp\left(\frac{\pi}{2}\sqrt{\frac{\mathrm{Pe}}{\eta}}\right) \right] \right\} \right) \coth \left(\frac{\pi}{4}\sqrt{\frac{\mathrm{Pe}}{\eta}} \right). \tag{33b}$$

With the change of variable $y = r - r_{f(S)}$, taking $c_A = G_A(y)$ (on account of steady state) and considering $r_{f(S)} \gg 1$ [which is valid given $\mathrm{Pe} > O(1)$], the steady state ($\partial / \partial t \equiv 0$) form of Eq. (7) for c_A in the vicinity of the stationary front transforms approximately into

$$\left(\frac{\eta \mathrm{Pe}}{r_{f(S)}^2} + 1 \right) \frac{d^2 G_A}{dy^2} - \mathrm{Pe}\, G_A(G_A + K_S y) = 0, \quad \text{with } G_A(y \to -\infty) \to -K_S y, \ G_A(\infty) = 0, \tag{34}$$

where $c_B = c_A - \theta = G_A(y) + K_S y$. The first boundary condition for G_A simply stems from the fact that as $y \to \infty$, i.e., as we move away from the front towards the origin, $c_B \to 0$ and thus one must have $c_A \to \theta$. We conduct another change of variables

$$G_A = \bar{\alpha}\bar{G}_A \equiv \frac{K_S^{2/3}}{\mathrm{Pe}^{1/3}}\bar{G}_A, \quad y = \bar{\beta}\bar{y} \equiv \frac{\bar{y}}{(\mathrm{Pe}\, K_S)^{1/3}}, \quad \text{where } \bar{\alpha} = \frac{K_S^{2/3}}{\mathrm{Pe}^{1/3}} \text{ and } \bar{\beta} = (\mathrm{Pe} K_S)^{-1/3} \tag{35}$$

with which Eq. (34) further transforms to

$$\left(\frac{\eta \mathrm{Pe}}{r_{f(S)}^2} + 1 \right) \frac{d^2 \bar{G}_A}{d\bar{y}^2} - \bar{G}_A(\bar{G}_A + \bar{y}) = 0, \quad \text{with } \bar{G}_A(\bar{y} \to -\infty) \to -\bar{y}, \quad \bar{G}_A(\infty) = 0, \tag{36}$$

Using Eq. (9), $\bar{R}_{(S)}$ may be evaluated as

$$\bar{R}_{(S)} = 4\pi \bar{\alpha}^2 \bar{\beta} \int_{-\infty}^{\infty} \bar{G}_A(\bar{y})[\bar{G}_A(\bar{y}) + \bar{y}](\bar{\beta}\bar{y} + r_{f(S)})^2 \, d\bar{y}. \tag{37}$$

Noting that $\bar{G}_A(\bar{G}_A + \bar{y})$ is an even function because of the nature of variations in c_A and c_B, we deduce that $\bar{G}_A(\bar{G}_A + \bar{y})\bar{y}$ must be an odd function, and hence Eq. (37) simplifies to

$$\bar{R}_{(S)} = 4\pi\bar{\alpha}^2\bar{\beta}\left(c_1\bar{\beta}^2 + \bar{k}r_{f(S)}^2\right), \quad c_1 = \int_{-\infty}^{\infty} \bar{G}_A(\bar{z})[\bar{G}_A(\bar{z}) + \bar{z}]\bar{z}^2 \, d\bar{z} \sim O(1), \tag{38}$$

with $\bar{k} = (\eta\mathrm{Pe}/r_{f(S)}^2 + 1)$. The constant c_1 may be evaluated numerically by solving Eq. (36) and then integrating using the expression given above. In deriving Eq. (38), we have used the following [from Eq. (34)]:

$$\int_{-\infty}^{\infty} \bar{G}_A(\bar{y})[\bar{G}_A(\bar{y}) + \bar{y}] \, d\bar{y} = \int_{-\infty}^{\infty} \left(\frac{\eta\mathrm{Pe}}{r_{f(S)}^2} + 1\right)\frac{d^2\bar{G}}{d\bar{y}^2} \, d\bar{y} = \left(\frac{\eta\mathrm{Pe}}{r_{f(S)}^2} + 1\right) = \bar{k}. \tag{39}$$

When $\mathrm{Pe} \geqslant O(1)$, $c_1\bar{\beta}^2 \ll r_{f(S)}^2$, and thus, $\bar{R}_{(S)}$ may be further approximated as

$$\bar{R}_{(S)} = 4\pi\bar{\alpha}^2\bar{\beta}\bar{k}r_{f(S)}^2 = 4\pi\coth\left(\frac{\pi}{4}\sqrt{\frac{\mathrm{Pe}}{\eta}}\right). \tag{40}$$

While evaluating the above expression, Eq. (32) has been used for $r_{f(S)}$.

It is important to note that although Eqs. (31) and (32) describe steady-state solutions for θ, the front location and the global reaction rate, respectively, c_C never reaches a steady state because it is continually produced by the reaction.

We shall now examine two limiting cases of the stationary solution: (1) the weak dispersion regime and (2) the strong dispersion regimes.

a. The weak dispersion regime $[r_{f(S)}^2 \gg \eta\mathrm{Pe}$ *and* $\eta \ll \mathrm{Pe}]$. Examining Eq. (31), we observe that under the conditions $r_{f(S)}^2 \gg \eta\mathrm{Pe}$ and $\eta \ll \mathrm{Pe}$, it may be approximated as

$$\theta_{(S)} = 1 - 2\exp\left(-\frac{\mathrm{Pe}}{r}\right). \tag{41}$$

In essence, the first condition implies that the steady-state reaction front resides in a region where molecular diffusion dominates over mechanical dispersion. With $\theta_{(S)}$ given as in Eq. (41), Eq. (32) yields for the front location:

$$r_{f(S)} = \frac{\mathrm{Pe}}{\ln 2} \gg \sqrt{\eta\mathrm{Pe}} \quad \text{when } \eta \ll \mathrm{Pe}. \tag{42}$$

For $\eta \ll \mathrm{Pe}$, Eq. (40) approximates as

$$\bar{R}_{(S)} = 4\pi, \quad \text{when } \eta \ll \mathrm{Pe}. \tag{43}$$

Note that Eq. (41) is simply the solution for θ in the dispersion-free scenario ($\eta = 0$), previously reported by Comolli *et al.* [37]. Therefore, in the weak-dispersion scenario the steady-state reaction front exhibits essentially the same behavior as in a dispersion-free case.

b. The strong dispersion regime $[\eta \gg \mathrm{Pe}]$. Now examining Eq. (32), we observe that for $\eta \gg \mathrm{Pe}$, which leads to the approximations: $e^{\pi\sqrt{\mathrm{Pe}}/2\sqrt{\eta}} \approx 1 + (\pi/2)\sqrt{\mathrm{Pe}/\eta}$ and $\ln[1 - (1 - e^{\pi\sqrt{\mathrm{Pe}}/2\sqrt{\eta}})/2] \approx (\pi/4)\sqrt{\mathrm{Pe}/\eta}$, this equation may be simplified as

$$r_{f(S)} = \sqrt{\eta\mathrm{Pe}}. \tag{44}$$

Thus, in this regime, the steady-state reaction front resides at a location where mechanical dispersion and molecular diffusion are of comparable strength. At the same time, for $\eta \gg \mathrm{Pe}$, Eq. (44) approximates for the steady-state reaction rate [from Eq. (40)]

$$\bar{R}_{(S)} = 16\sqrt{\eta/\mathrm{Pe}}, \quad \text{when } \eta \gg \mathrm{Pe}. \tag{45}$$

An alternative derivation of the scalings estimates for $\bar{R}_{(S)}$ (in terms of η and Pe) has been included in Appendix F.

Based on the discussions in Sec. III B 3 a and III B 3 b, several major inferences may be drawn, which are summarized below:

(i) When $\eta \ll$ Pe (weak dispersion), the steady-state reaction front resides at a location where mechanical dispersion is negligible compared to molecular diffusion. For this scenario, the steady-state (normalized) global reaction rate ($\bar{R}_{(S)}$) is independent of both η and Pe.

(ii) Conversely, when $\eta \gg$ Pe (strong dispersion), the steady-state reaction front is at a location where mechanical dispersion is comparable to molecular diffusion, characterized by $r_f \sim \sqrt{\eta \text{Pe}}$. In this case, in stark contrast to the weak dispersion scenario, the (normalized) global reaction rate depends on both η and Pe [see Eq. (45)].

(iii) Furthermore, comparing the limiting expressions for $\bar{R}_{(S)}$ in the weak [Eq. (43)] and the strong [Eq. (45)] dispersion scenarios, we observe that the global reaction rate will always be higher for $\eta \gg$ Pe than for $\eta \ll$ Pe. Therefore, it is expected that strong mechanical dispersion will leave a permanent mark on all the reaction front's properties, even in the steady state, while also enhancing the global reaction rate.

However, the steady-state reaction front will never reside in a region where mechanical dispersion is dominant over molecular diffusion, regardless of how strong dispersion is.

4. The transition times

a. Transition time to the steady state (t_{SS}). At sufficiently large times, the reaction front reaches a steady state (as discussed in Sec. III B 3) and this timescale of transition to the stationary state (t_{SS}) may be estimated by combining the results of Sec. III B 1 and Sec. III B 3. This is achieved by simply equating the transient front location ($r_f(t)$) to its steady-state position ($r_{f(S)}$), given by Eq. (32).

In the strong dispersion scenario, from Eq. (15) it follows that $r_f = 0.914 \, \eta^{1/4} t^{1/4}$, while from Eq. (44) we note that $r_{f(S)} = \sqrt{\eta \text{Pe}}$. Hence, t_{SS} in this scenario may be estimated from $0.914 \eta^{1/4} t_{SS}^{1/4} = \eta^{1/2} \text{Pe}^{1/2}$, which yields $t_{SS} = 1.43 \, \text{Pe}^2 \eta$. On the other hand, in the weak dispersion scenario ($\eta \ll$ Pe), the front transitions from a dispersion-dominated regime into the diffusion-dominated regime before it reaches the steady state (see the discussion in the next paragraph, Appendix E, and Sec. III B 6). Therefore, at large times, the transition actually occurs from the diffusion-dominated regime to the stationary state. In the former regime, $r_f = 3^{1/3} t^{1/3}$ [see Eq. (E3)], while in the steady state, $r_{f(S)} = [\ln(2)]^{-1} \text{Pe}$ and hence t_{SS} for the weak dispersion scenario is estimated from $3^{1/3} t_{SS}^{1/3} = [\ln(2)]^{-1} \text{Pe}$, which yields $t_{SS} = 3^{-1/3} [\ln(2)]^{-1} \text{Pe}^3 \approx \text{Pe}^3$. The above results are summarized as

$$t_{SS} = \begin{cases} \text{Pe}^3, & \text{when } \eta \ll \text{Pe} \\ 1.43 \, \eta \text{Pe}^2. & \text{when } \eta \gg \text{Pe} \end{cases}. \tag{46}$$

Evidently, the presence of sufficiently strong dispersion (characterized by $\eta \gg$ Pe) delays the onset of the steady state (since $1.43 \, \eta \text{Pe}^2 \gg \text{Pe}^3$ when $\eta \gg$ Pe), while this transition time is independent of the dispersivity length when it is sufficiently weak ($\eta \ll$ Pe). An alternative derivation for the scalings of t_{SS} is presented in Appendix G, which yields the same scaling expectations as presented in Eq. (46).

The steady-state transition time t_{SS} may also be computed numerically (say, $t_{SS}^{\text{num}(k)}$) by simply estimating the time instance when the front position r_f is sufficiently close to its steady-state location $r_{f(S)}$ (i.e., $r_f = k r_{f(S)}$, where k is a numerical factor close to 1), as follows:

$$t_{SS}^{\text{num}(k)} = t|_{r_f = k r_{f(S)}}. \tag{47}$$

In Eq. (47), the factor k (taken as 0.9 in this study) quantifies how close the transient numerical solution for the reaction front position is to the steady state.

b. Transition time between the dispersion and the diffusion-dominated regimes (t_{trans}). In a spherically advected reaction front, mechanical dispersion always dominates over molecular diffusion at sufficiently small times. However, in Sec. III B 3 a, it has been demonstrated that in the steady state and for weak dispersion ($\eta \ll$ Pe), the front resides in a region where diffusion dominates over dispersion. Therefore, it is expected that for weak dispersion, the front will undergo a transition from the dispersion-dominated into the diffusion-dominated regime at an earlier time (say, t_{trans}), before reaching the stationary state. An estimate for the scaling of this transition time may be inferred by noting that in the diffusion-dominated regime, the front advances as $r_f = (3t)^{1/3}$ [Eq. (E3)], and therefore the front moves into the diffusion-dominated region (i.e., the front position crosses the radial distance $\eta^{1/2}\text{Pe}^{1/2}$) at the time

$$t_{\text{trans}} = (1/3)\eta^{3/2}\text{Pe}^{3/2}. \tag{48}$$

A numerical estimate for t_{trans} may be deduced by computing the time instance (say, $t_{\text{trans}}^{\text{num}}$) when the front position satisfies $r_f = \sqrt{\eta\text{Pe}}$:

$$t_{\text{trans}}^{\text{num}} = t|_{r_f=\sqrt{\eta\text{Pe}}}. \tag{49}$$

Note that when $\eta >$ Pe (i.e., in the strong dispersion scenario), the front actually reaches, and saturates at, $\sqrt{\eta\text{Pe}}$. This, however, does not represent a true transition point simply because the front does not proceed any further, and thus Eq. (49) does not apply to situations when $\eta >$ Pe.

5. Transient reaction front behavior

Figure 2 depicts the numerical solutions for the temporal evolution of the front properties and the mass of the product, for various choices of η (including $\eta = 0$, represented by the black curves) for Pe $= 10^0$. The dashed lines represent the analytical approximations for the front properties and the product mass as deduced in Sec. III B 1 and Sec. III B 2, while their temporal scalings are also depicted (floating solid lines for the dispersion-dominated regimes and floating dashed-dot lines for the diffusion-dominated reaction-limited regime). The dotted horizontal lines indicate the front properties in the steady state. We first observe that the analytical estimates (summarized in Table II) compare well with the numerical solutions for all the front properties as well as the mass of the product. Furthermore, all transient solutions are seen to asymptotically approach the stationary solution at sufficiently large times.

Examining Fig. 2(a), we note that the dispersive and the dispersion-free ($\eta = 0$) solutions approach each other after the transition region $r_f \sim \sqrt{\eta\text{Pe}}$ when $\eta \leqslant$ Pe $= 1$ (implying weak mechanical dispersion), wherein the transition occurs at a smaller radial distance than the stationary front location, i.e., $r_{f(S)} > \sqrt{\eta\text{Pe}}$. On the other hand, when $\eta >$ Pe $= 1$, the cross-over point $r^2 = \eta\text{Pe}$ gets pushed radially outward and is at a distance comparable to the location of the stationary front. Thus, dispersion leaves a permanent mark on the reaction front, as expected from Eq. (44) and the discussion in Sec. III B 3 b. One further observes that dispersion always results in a faster front movement as compared to the dispersion-free scenario. Moreover, the inset of Fig. 2(a) shows that the quantity $t^{-1/4}r_f(t)$ indeed scales as $\eta^{1/4}$, as predicted by Eq. (15), which provides further confirmation for the early-time approximations derived in Sec. III B 1.

Examining the other three panels in Fig. 2, the reaction width, the global reaction rate, and the mass of the product are also found to follow similar patterns as that of the front position, r_f; that is, for weak dispersion ($\eta \ll$ Pe), they all approach the diffusion-dominated reaction-limited regime before the steady state settles, while in the case of strong dispersion ($\eta \gg$ Pe), all front properties remain distinct from the dispersion-free scenario ($\eta = 0$), as mechanical dispersion indelibly influences the reactive mixing process. For all values of η, the dispersion-dominated reaction-limited regime (characterized by $r_f \sim t^{1/4}$, $\bar{R} \sim t^{3/4}$, $w_f \sim t^{1/4}$) appears at early times in all four panels. On the other hand, for $\eta = 10^4$ and 10^6, the condition in Eq. (25) is satisfied, and therefore we indeed observe a brief window ($t > 1$) during which the dispersion-dominated mixing-limited regime (characterized by $r_f \sim t^{1/4}$, $\bar{R} \sim t^{-1/4}$, $w_f \sim t^{-1/12}$) materializes. The insets in Figs. 2(b), 2(c),
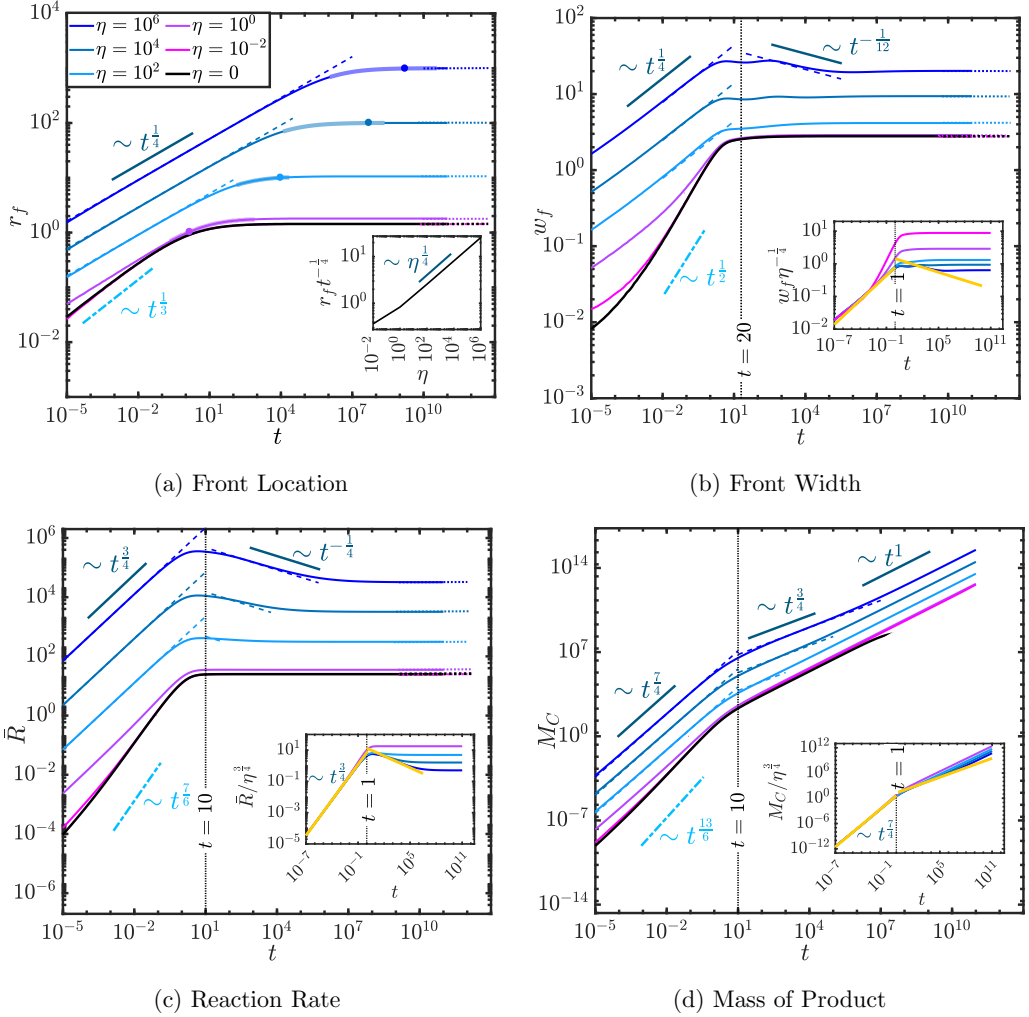
(a) Front Location

(b) Front Width

(c) Reaction Rate

(d) Mass of Product

FIG. 2. Time evolution of the front properties and product mass, for various choices of η (= 0, 0.01, 1, 10^2, 10^4, and 10^6) and Pe = 1; the dotted lines represent the stationary solution [Eq. (32) in (a), Eq. (40) in (c), and the numerical stationary solution in the other panels]. The legend presented in (a) applies to all panels. The circular markers in (a) represent the transition point $r_f = \sqrt{\eta \mathrm{Pe}}$ (with the shaded region surrounding it approximating the range $r_f = \sqrt{\eta \mathrm{Pe}}/2$ to $r_f = 2\sqrt{\eta \mathrm{Pe}}$); the dashed lines in panel (a) represent r_f as per Eq. (15); the dashed lines in (b) to (d) represent w_f, $\bar{R}$, and M_C, respectively, as per Eqs. (19) to (21) for $t < 10$ and Eqs. (28) to (30) for $t > 10$; the inset in (a) shows $r_f t^{-1/4}$ vs η for $t \ll 1$, while those in (b), (c), and (d), respectively, show $w_f \eta^{-1/4}$, $\bar{R} \eta^{-3/4}$, and $M_c \eta^{-3/4}$ vs t for the above choices of η; the yellow lines in the inset in panels (b), (c), and (d), respectively, represent $0.78\,t^{1/4}$, $6.30\,t^{3/4}$, and $3.60\,t^{7/4}$ for $t < 1$ and $1.438\,t^{-1/12}$, $13.27\,t^{-1/4}$, and $17.69\,t^{3/4}$ for $t > 1$.

and 2(d) indicate that at early times, the curves for $w_f \eta^{-1/4}$, $\bar{R}\eta^{-3/4}$ and $M_c\eta^{-3/4}$ corresponding to the various choices of η collapse onto single curves following their respective temporal scalings, as predicted by Eqs. (19)–(21) and (28)–(30). Furthermore, the global reaction rate reaches its maximum at $t \sim O(1)$ once the reaction-limited regime is over (see Sec. III B 2), and hence it is expected to follow the same temporal behavior outlined in Sec. III B 1 during this period, which indicates that the maximum in $\bar{R}$ should also scale as $\eta^{3/4}$ according to Eq. (19) as is indeed recovered from the numerical simulations.
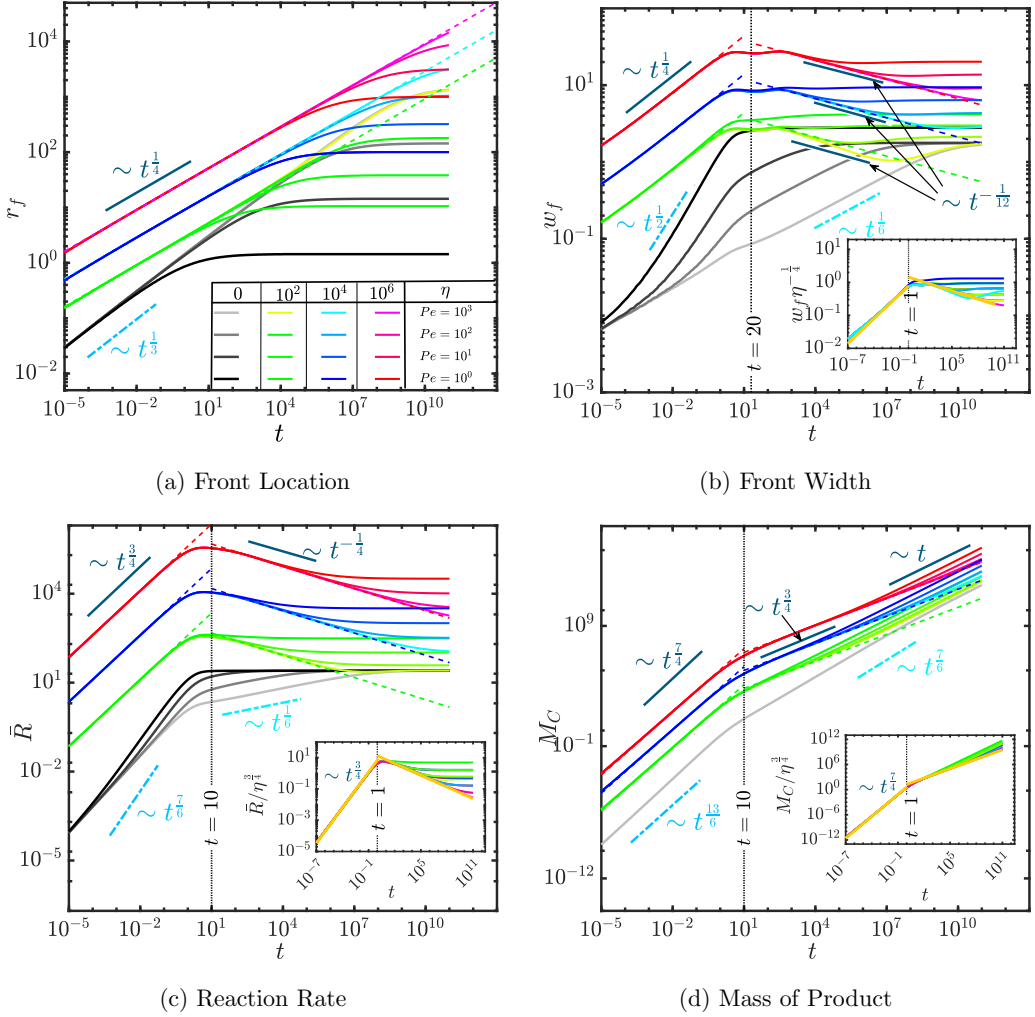
(a) Front Location

(b) Front Width

(c) Reaction Rate

(d) Mass of Product

FIG. 3. Time evolution of the front properties and product mass, for various choices of Pe ($= 1, 10, 10^2$, and 10^3) and η [$= 0$ (no dispersion), 10^2, 10^4, and 10^6]; the legend presented in Fig. 2(a) applies to all panels. The line descriptions are the same as for Fig. 2. The insets in panels (b), (c), and (d) are analogous to their counterparts in Fig. 2.

Figure 3 illustrates the same front properties as in Fig. 2 for various choices of Pe ($= 1, 10, 100$, and 1000) and four choices of η ($10^6, 10^4, 10^2$, and 0); the colored lines represent the results for dispersive ($\eta > 0$) front movement, and the gray curves denote nondispersive ($\eta = 0$) transport. The analytical solutions reported in Sec. III B 1, Sec. III B 2, and Appendix E, along with the temporal scalings are also shown, and they agree well with the numerical solutions in all the panels. As expected, there are a number of qualitative similarities between Figs. 2 and 3. At small times ($t < 1$), the dispersion-dominated reaction-limited regime (characterized by $r_f \sim t^{1/4}$, $w_f \sim t^{1/4}$, $\bar{R} \sim t^{3/4}$, and $M_C \sim t^{7/4}$) is apparent for $\eta > 0$, while for $\eta = 0$, the diffusion-dominated reaction-limited regime ($r_f \sim t^{1/3}$, $w_f \sim t^{1/3}$, $\bar{R} \sim t^{7/6}$ and $M_C \sim t^{13/6}$; see Appendix E) also appears clearly. Interestingly, for all choices of η, the early-time reaction-limited regime is largely insensitive to Pe, except for the reactive front's width [panel 3(b)] which shows a weak dependence on Pe when $\eta = 0$. We further observe that for Pe $< \eta$, the dispersive and the nondispersive

solutions for all the front properties differ at all times, while for $Pe \gtrsim \eta$ (see, for instance, the cases $Pe = 10^3$, $\eta = 10^2$, and $Pe = \eta = 10^2$), the front's behavior asymptotically approaches that for $\eta = 0$ (dispersion-free scenario) before the front reaches the steady state, thus indicating a transition into the diffusion-dominated regime from a dispersion-dominated one.

It is evident that larger values of Pe delay the onset of the steady state [as expected from Eq. (46)], while also pushing the steady-state front location radially outward, as evident from Eqs. (42) and (44). On the other hand, dispersion only impacts this onset time when it is sufficiently strong [$\eta > Pe$; also see Fig. 2(a)], and as such, the presence of dispersion also delays the commencement of the steady-state regime, as indeed is established in Sec. III B 4 a; see Fig. 7 and Appendix H for further discussion on the various transition times.

Importantly, now the presence of the dispersion-dominated mixing-limited regime (see Sec. III B 2) becomes prominent when $t > 1$, especially for relatively larger values of η and Pe, for which the condition (25) is satisfied. Concomitantly, the mixing-limited regime for the dispersion-free scenario ($\eta = 0$, $r_f \sim t^{1/3}$, $w_f \sim t^{1/6}$, $\bar{R} \sim t^{1/6}$, and $M_C \sim t^{7/6}$) as established by Comolli *et al.* [37] also materializes at the intermediate times. It is to be noted that the front still moves as $r_f \sim t^{1/4}$, despite the fact that $t > 1$ and as asserted in Sec. III B 2, the global reaction rate and the front width both decay with time ($\bar{R} \sim t^{-1/4}$, $w_f \sim t^{-1/12}$) and approach their steady-state values form above. As a consequence, the mass of the product grows as $t^{3/4}$, as shown in panel 3(d). Furthermore, the global reaction rate indeed goes through a maximum at $t \sim O(1)$ for all choices of Pe and η, thus confirming the inferences of Sec. III B 2. The front width, on the other hand, exhibits two maxima, especially for larger values of η, which is a consequence of its definition in Eq. (8). We have verified (not shown here for the sake of brevity) that alternative definitions of w_f [e.g., normalized second moment considering the front to be approximately planar, i.e., same as Eq. (8) but without the $4\pi r^2$ in the denominator and the numerator] exhibit the same temporal scalings as the original definition [Eq. (8)], while going through only one maxima in their respective transiences. It is also worth noting that for relatively smaller values of η and Pe, such as $Pe = 1$ and $\eta = 100$, the mixing-limited regime does not materialize, simply because the condition (25) is not truly met for these values. Finally, we reiterate that the mixing-limited regime pans out very differently in the absence of mechanical dispersion regardless of the Pe value (here $\bar{R}$ and w_f both continually increase with time), as evident from the curves corresponding to $\eta = 0$ in Fig. 3, which underlines another major qualitative difference between a dispersive and a nondispersive front.

6. Steady-state reaction front behavior

Figure 4 demonstrates the variations in θ at steady state for various choices of η (see legend) for $Pe = 1$ in Fig. 4(a) and $Pe = 10^3$ in Fig. 4(b). The orange vertical lines demarcate the boundary between the dispersion-dominated and the nondispersive (or diffusion-dominated) regions, i.e., the cross-over point $r^2 = \eta Pe$. When $\eta < Pe$, the solution for θ matches the dispersion-free counterpart [Eq. (41); green curve in Fig. 4] exactly, while at the same time it also lies to the right of its respective orange line, indicating that the front is located in the nondispersive region. When $\eta > Pe$, however, we observe that $\theta_{(S)}$ deviates significantly from its dispersion-free counterpart. While the front is located further forward, it actually resides [now $r_{f(S)} \sim \sqrt{\eta Pe}$; see Eq. (44)] in the vicinity of the cross-over point, i.e., well within the transition region between the nondispersive and the dispersion-dominated regimes.

The insets illustrate the steady-state variations in the reactant concentrations and the maximum-normalized local reaction rate (R) for $\eta = 0$ (solid lines) and $\eta = 10^7$ (dotted lines). Examining the inset in Fig. 4(a), we observe that the presence of dispersion causes significantly reduced concentration of the reactants in a relatively large region near the stationary front, although the global stationary reaction rate is still found to be higher in presence of dispersion than otherwise. This occurs because the stationary reaction front is located more than three orders of magnitude ahead for $\eta = 10^7$ than that for the dispersion-free scenario ($\eta = 0$) and hence, despite the local reaction rate at the front being smaller in magnitude for $\eta = 10^7$, the cumulative reaction rate is still
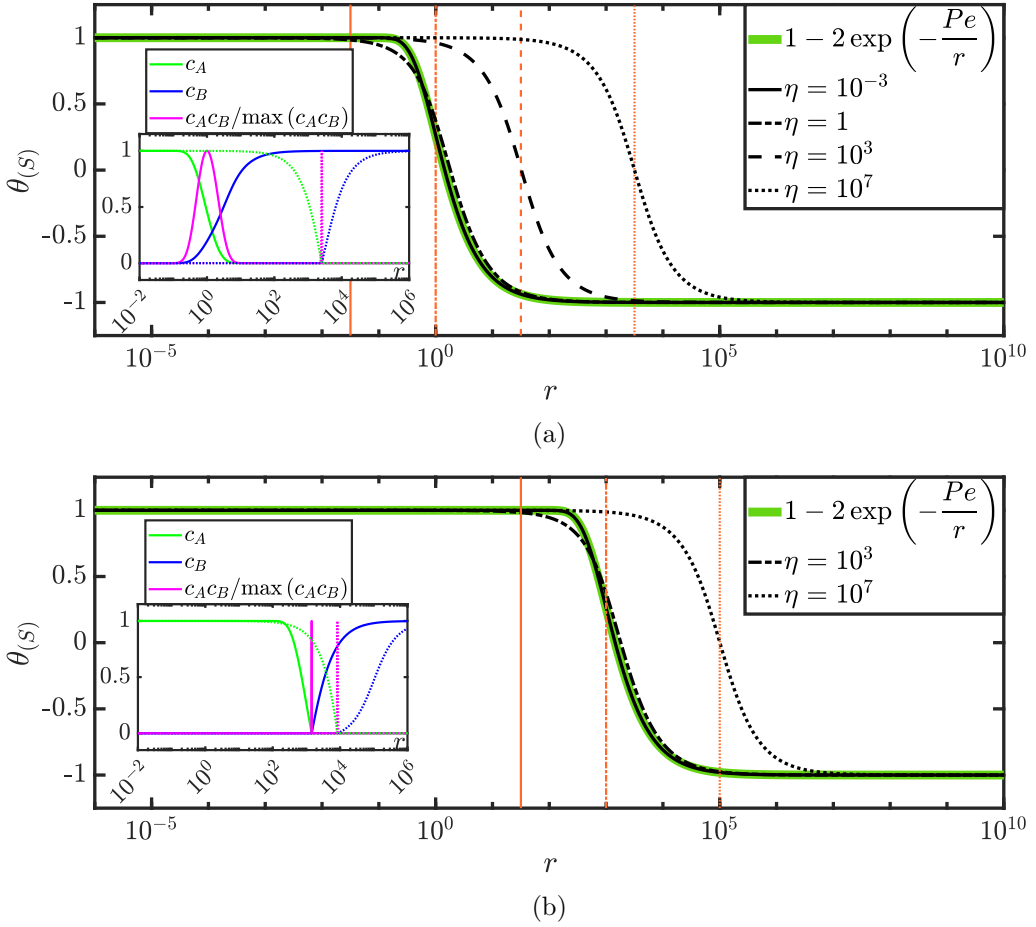
FIG. 4. Radial profile of the stationary solution of θ ($= c_A - c_B$); the vertical orange lines represent the cross-over point $r = \sqrt{\eta \text{Pe}}$, associated with the respective η value based on the line style (see legends). The numerical stationary solution for $c_A - c_B$ matches exactly the closed-form expression in Eq. (31). The stationary profiles for the concentrations of reactants and the maximum-normalized local reaction rate are presented in the insets, where the solid lines correspond to $\eta = 0$ and the dotted lines correspond to $\eta = 10^7$. (a) Steady state, Pe $= 1$ and (b) Steady state, Pe $= 10^3$.

larger because the reaction zone is spread out over the surface of a larger sphere. Figure 4(b) and its inset reveal that for a larger Pe (Pe $= 10^3$), the steady-state front gets pushed further ahead, while the reactant concentrations also get smaller, for both $\eta = 0$ and $\eta = 10^7$. The general characteristics discussed as above remains unchanged for Pe $= 10^3$, although now the enhancement caused by dispersion with respect to the $\eta = 0$ scenario is relatively smaller.

Figure 5 illustrates the enhancement of the steady-state global reaction rate ($\bar{R}_{(S)}$) for $\eta > 0$ with respect to the dispersion-free scenario (steady-state global reaction rate $\bar{R}_{(S)}^0$ for $\eta = 0$) as a color map in the (Pe, η) parameter space, computed numerically from the stationary solutions of c_A and c_B. $\bar{R}_{(S)}$ is observed to be greatly enhanced above the Pe $= \eta$ curve, which corresponds to a strong dispersion scenario and hence results in the steady-state front residing between the dispersion-dominated and the nondispersive regions, in agreement with Figs. 2 and 3. Furthermore, the relative magnification in the global reaction rate seems to be larger for smaller Pe values and larger η values, which is in agreement with the scalings obtained by comparing Eqs. (43) and (45),
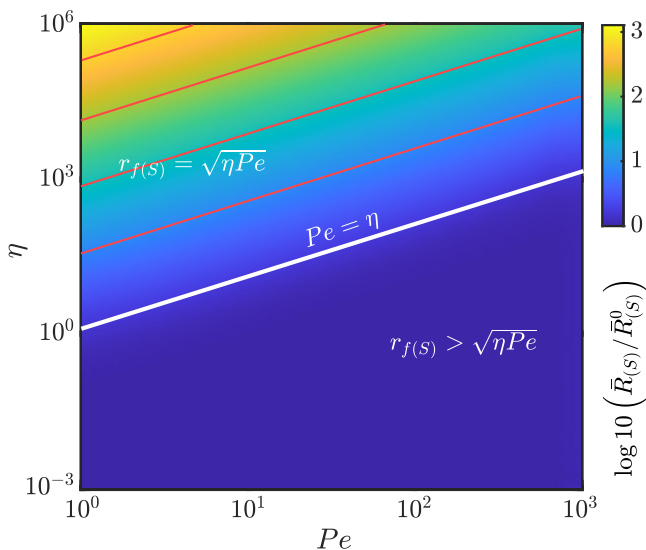
FIG. 5. Color map of the normalized steady-state global reaction rate normalized by its value in the dispersion-free scenario, in the (Pe, η) parameter space. The thin red lines above and parallel to the white line are η/Pe isolines (where η/Pe = const).

as well as with Fig. 3(c). In particular, Eq. (45) indicates that $\bar{R}_{(S)}$ is a function of η/Pe only for $\eta >$ Pe. This feature is reflected in the region above the white line in Fig. 5, where we can observe that the red lines drawn parallel to the white line (i.e., those corresponding to η/Pe = constant) indeed represent the constant contour lines with adequate accuracy. On the other hand, below the $\eta =$ Pe line, there is practically no enhancement in the steady-state reaction rate, thus indicating that there is very little separating a dispersive front from a nondispersive front in this scenario.

Figure 6 depicts the variations in the stationary front's location normalized by Pe [$r_{f(S)}$/Pe, in Fig. 6(a)], and the steady-state global reaction rate [$\bar{R}_{(S)}$, Fig. 6(b)] as functions of η/Pe, as computed from the numerical solutions of the steady-state version of Eq. (6). Examining both the panels, we observe that both $r_{f(S)}$/Pe and $\bar{R}_{(S)}$ are indeed independent of η/Pe in the weak dispersion regime, when η/Pe $\ll 1$, while they scale as $\sqrt{\eta/\text{Pe}}$ when dispersion is strong (η/Pe $\gg 1$), as expected from Eqs. (42) and (44) for $r_{f(S)}$, and Eqs. (43) and (45) [or Eq. (40)] for $\bar{R}_{(S)}$ in Sec. III B 3 a and Sec. III B 3 b.

Figure 7 presents the (numerically generated) phase diagram for the reactive transport regimes of spherically advected reaction fronts for Pe = 10. It summarizes the temporal scalings of the front properties and the product mass for the various transient regimes as noted in Table II, along with the stationary state scalings in terms of η and Pe as inferred from Eqs. (42) and (44) for the front location and from Eqs. (43) and (45) for the global reaction rate. The dotted horizontal line represents $\eta =$ Pe, and the dotted vertical line shows the instant $t = 1$. The red curve depicts the transition time (termed as t_{trans}) between the dispersion-dominated and the diffusion-dominated (nondispersive) regions and indeed exhibits a scaling $t_{\text{trans}} \sim \text{Pe}^{3/2}\eta^{3/2}$, as demonstrated in Sec. III B 4 b. Six distinct regimes are clearly visible in the (t, η) plane: (1) the dispersion-dominated reaction-limited regime at early times (dark pink; see Sec. III B 1), (2) the diffusion-dominated reaction-limited regime (dark violet) when dispersion is sufficiently weak (see Appendix E), (3) a gray region that demarcates the transition from the diffusion-dominated regime into the steady-state behavior at long times, (4) a dispersion-dominated mixing-limited regime (yellow; see Sec. III B 2) above the $\eta =$ Pe curve at times sufficiently large ($t > 1$) but before the steady state has settled ($t < t_{SS}$), (5) the dispersion-dominated steady-state regime (blue; see Sec. III B 3 b), and (6) the diffusion-dominated steady-state
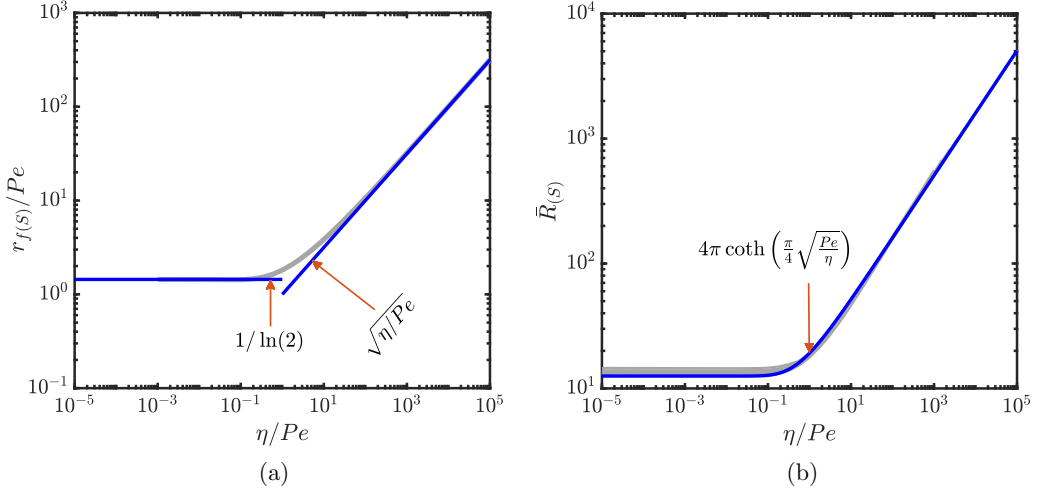
FIG. 6. Variations of (a) stationary front location normalized by Pe (i.e., $r_{f(S)}/\text{Pe}$), and (b) steady-state global reaction rate $\bar{R}_{(S)}$, as functions of η/Pe; the black curves are obtained from the numerical steady-state solution [i.e., the solution of Eq. (6) with $\partial c_i/\partial t$ set to zero]; the analytical expressions for the limiting scenario of $\eta \ll \text{Pe}$ [Eq. (42)] and $\eta \gg \text{Pe}$ [Eq. (44)] are shown as blue lines in (a). In (b) the blue line indicates the analytical solutions for $\bar{R}_{(S)}$ from Eq. (40).

behavior (green; see Sec. III B 3 a). The boundaries of the two steady-state regions (representing the transition time to the steady state, t_{SS}) have been obtained from the numerical solutions. The profile of this boundary aptly reflects the scaling expectations derived in Eq. (46), i.e., when $\eta \ll \text{Pe}$ (weak dispersion), t_{SS} is independent of η, while $t_{SS} \sim \eta$ when $\eta \gg \text{Pe}$ (strong dispersion). Furthermore, we have observed (although not shown here for the sake of brevity) that for other values of Pe as well, the qualitative nature of the phase diagram remains the same: For larger values of Pe, the red
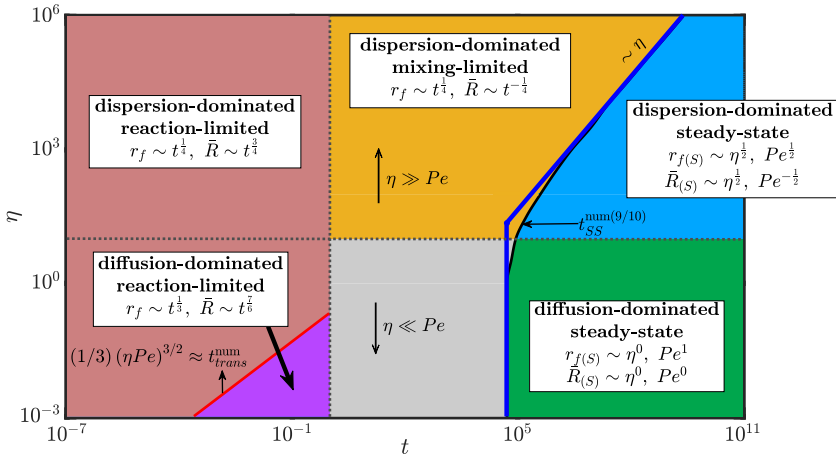

FIG. 7. Phase diagram for the reactive transport regimes of spherically advected reaction fronts for Pe $= 10$, as a function of time and η. Both transient and steady-state regimes are indicated. The exxpected temporal scalings for the transient regimes are summarized in Table II, and the scaling for the transition times may be found in Sec. III B 4. No particular scaling can be expected for the gray region. The curves corresponding to the transition time t_{trans} and the steady-state time t_{SS}, as obtained from the numerical solutions, are also presented.

curve delimiting the upper boundary of regime (2) (the violet region) is pushed further downward because of weaker molecular diffusion, while the steady-state regime [regions (5) and (6)] also moves farther to the right because of delayed onset of the stationary state, and vice versa for smaller values of Pe. Illustrative examples showing the variations in the transition times (t_{SS} and t_{trans}) with Pe are included in Appendix H; they confirm the scaling expectations outlined in Eqs. (46) and (48).

Concerning transition times, it should be further noted that simply equating the reaction rates in Eqs. (19) and (28) yields a transition time $t^\star = 2.1$ in the global reaction rate ($\bar{R}$) (applicable when dispersion is sufficiently strong; see Sec. III B 2). Indeed, it is expected that t^* will be $O(1)$ as it essentially marks the front's transition from a reaction-limited regime (Sec. III B 1) to a mixing-limited regime (Sec. III B 2) and given that the reaction timescale has been chosen as the characteristic timescale here.

The phase diagram in Fig. 7 clearly shows that for sufficiently strong dispersion, when $\eta \gg$ Pe (along with $\eta \gg 1$), the front never experiences a diffusion-dominated regime and will directly transition to the stationary state after passing through the early-time dispersion-dominated reaction-limited and the intermediate-time mixing-limited regimes, respectively. The reactive transport for such scenarios will thus be under the influence of mechanical dispersion at all times. However, when the condition ηPe $\gg 1$ is not rigorously satisfied, the mixing-limited regime may become weak and confined only to a small time window at intermediate times. On the other hand, when $\eta \ll$ Pe (weak dispersion), the front starts in the dispersion-dominated reaction-limited regime [regime (1)], then transitions into the diffusion-dominated reaction-limited regime [regime (2)], and subsequently reaches the steady state [regime (6)] at large times after passing through the gray region of the diagram. As a consequence, the steady-state front no longer remains under the influence of mechanical dispersion. In addition, in this scenario, despite mechanical dispersion being active at early times, it is not sufficiently strong to enforce the mixing-limited regime, otherwise realized for larger values of η.

IV. CONCLUSION

We have studied the dynamics of a spherically advected bimolecular reactive front with a $A + B \rightarrow C$ type chemical reaction in the presence of mechanical dispersion. The solution containing the species A is being injected into a porous medium initially saturated with a solution containing the species B. The governing equations are solved numerically, and analytical approximations are also derived; they uncover hitherto unknown reactive mixing regimes, which are different from to those previously found based on the conventional constant diffusion coefficient assumption.

At early times, mechanical dispersion dominates over molecular diffusion and the front goes through a reaction-limited regime, wherein the presence of dispersion significantly augments the reaction rate and product mass. We find that the front's mean position scales in time as $t^{1/4}$, as opposed to the $t^{1/3}$ behavior previously demonstrated for dispersion-free scenarios. On the other hand, at sufficiently large times, the reaction front approaches a steady state, wherein the front properties and reactant concentrations do not change with time. The transition from the dispersion-dominated behavior to the nondispersive behavior occurs at $r_f \sim \sqrt{\eta \text{Pe}}$. Hence, if the steady state is reached before the said transition, mechanical dispersion will have a permanent impact on the front properties and will thus result in a lasting augmentation of the reaction rate. Evidently, this is feasible only when mechanical dispersion is sufficiently strong, characterized by the condition $\eta > $ Pe. In such cases, once the steady state has been established, the front always resides in a region where mechanical dispersion and molecular diffusion are of comparable strength ($r_f \sim \sqrt{\eta \text{Pe}}$) and this transition to the stationary state occurs at $t_{SS} \sim \eta \text{Pe}^2$.

When ηPe $\gg 1$, i.e., when either dispersion or advection is sufficiently strong as compared to molecular diffusion, the reaction front may also go through a dispersion-dominated mixing-limited phase at intermediate times before reaching the steady state. During this phase, the global reaction rate and the front width continually decay with time and eventually approach their steady-state values. It is essential for mechanical dispersion to be present for this previously unreported regime to

exist: It cannot occur in purely diffusive (or diffusion-dominated) fronts, regardless of how large the Péclet number is. For weak dispersion, on the other hand, the front transitions into the nondispersive region well before the steady state settles, and thus, at large times, the relative differences in the front properties between the dispersive and the nondispersive scenarios become negligible. When $\eta <$ Pe, the transition from the dispersion-dominated to the diffusion-dominated regime occurs at $t_{\text{trans}} \sim \eta^{3/2}\text{Pe}^{3/2}$, while the onset of the stationary state occurs approximately at $t_{SS} \sim \text{Pe}^3$, independently of η. In the steady state, significant augmentation in the reaction rate (as compared to that in a dispersion-free scenario) comes about only when $\eta >$ Pe, i.e., for strong dispersion. This results in the normalized steady global reaction rate ($\bar{R}_{(S)}$) scaling as $\bar{R}_{(S)} \sim \eta^{1/2}\text{Pe}^{-1/2}$. On the contrary, in the weak dispersion scenario ($\eta <$ Pe), $\bar{R}_{(S)}$ is independent of both η and Pe.

We have thus established the conditions under which hydrodynamic dispersion affects the dynamics of spherical reaction fronts. The nonuniformity in the local dispersion coefficient resulting from its linear velocity dependence leads to novel scaling laws and enhanced reaction rates, which are different from the scalings predicted based on the conventional constant diffusion coefficient hypothesis. These findings hence provide fundamental insights into reactive fronts dynamics and will guide the development of reactive transport models for a broad range of applications that involve local injection of fluids in porous media.

APPENDIX A: DISCUSSION OF THE HYDRODYNAMIC DISPERSION TENSOR IN EQ. (1)

The hydrodynamic dispersion tensor ($\mathbf{D}^*$) is the sum of the molecular diffusion tensor ($\mathbf{D}_M^* = D_M\mathbf{I}$, assumed to be isotropic) and the mechanical dispersion tensor ($\tilde{\mathbf{D}}$), which accounts for solute spreading due to the interaction between transverse molecular diffusion and advection by the heterogeneous pore scale velocity field. Thus, $\mathbf{D}^* = \mathbf{D}_M^* + \tilde{\mathbf{D}}$, $\tilde{\mathbf{D}}$ being defined at asymptotically large times ($t' \to \infty$) as [1]

$$\tilde{\mathbf{D}} = \lim_{t \to \infty} \frac{d}{dt'}\{\langle[\mathbf{x}'(t') - \langle\mathbf{x}'(t')\rangle][\mathbf{x}'(t') - \langle\mathbf{x}'(t')\rangle]\rangle\}, \tag{A1}$$

where $\langle\cdot\rangle$ indicates an ensemble average over all solute particles and $\mathbf{x}'(t')$ is the position of such a particle at time t'.

In narrow confinements (such as tubes, or the space between parallel plates), the diffusion time across the channel cross section is much shorter than the residence time of a particle in the channel, which leads to a well-mixed solute concentration field within the confinement and results in $\tilde{D}_{ij} \sim v_c^2$ [49], where v_c is the characteristic velocity in the channel. This is known as Taylor dispersion.

On the other hand, for flow in porous media, the residence time within a pore is often comparable to the timescale of diffusion across it, and thus solute transport in such scenarios is characterized by incomplete mixing across pores. This results in $\tilde{D}_{ij} \sim v_c$ [49], i.e., mechanical dispersion becomes proportional to the local velocity. The most general expression for a second rank tensor, which is a linear function of a vector (i.e., $\mathbf{v}'$), is

$$\tilde{\mathbf{D}} = \lambda_1||\mathbf{v}'||\mathbf{I} + \lambda_2\frac{\mathbf{v}'\mathbf{v}'}{||\mathbf{v}'||}, \tag{A2}$$

where λ_1 and λ_2 are scalars with the dimensions of length. The hydrodynamic dispersion tensor in Eq. (1) follows directly from here. The linear relation between $\tilde{\mathbf{D}}$ and $\mathbf{v}'$ in Eq. (A2) [or Eq. (1)]

has been verified experimentally by several independent studies [50–54], and therefore it is well established in the literature [41,49,55] as an appropriate model for dispersion in porous media.

APPENDIX B: A BRIEF DERIVATION OF THE ADRE (3)

The upscaled (i.e., the Darcy scale) equation for the conservation of solute mass in a porous media may be expressed as [1,49]

$$\frac{\partial c'}{\partial t'} + \nabla' \cdot \mathbf{J}' = R(c'; \mathbf{x}', t'), \tag{B1}$$

where $c'(\mathbf{x}', t')$ is the Darcy scale concentration (i.e., volume averaged over a representative elementary volume of the pore space), $\mathbf{J}'$ is the Darcy scale flux, and R is the instantaneous (local) rate of reaction. The Darcy scale flux may be written as $\mathbf{J}' = \mathbf{J}'_{\text{adv}} + \mathbf{J}'_{\text{diff}} + \mathbf{J}'_{\text{disp}}$, where $\mathbf{J}'_{\text{adv}}$, $\mathbf{J}'_{\text{diff}}$, and $\mathbf{J}'_{\text{disp}}$ are, respectively, the advective, diffusive, and dispersive components of the fluxes. It is to be noted that $\mathbf{J}'_{\text{disp}}$ is a consequence of the upscaling process from the pore scale and the variabilities in the concentration and velocity at that scale [1]. These three components may be expressed, respectively, as $\mathbf{J}'_{\text{adv}} = \mathbf{v}'c'$, $\mathbf{J}'_{\text{diff}} = -\mathbf{D}^*_M \cdot \nabla'c'$ (Fick's law of diffusion) and $\mathbf{J}'_{\text{disp}} = -\tilde{\mathbf{D}} \cdot \nabla'c'$, where $\tilde{\mathbf{D}}$ is the mechanical dispersion tensor; see Appendix A. Enforcing these expressions into Eq. (B1), noting that $\nabla' \cdot \mathbf{v}' = 0$ on account of continuity (i.e., fluid mass conservation upscaled to the Darcy scale), and defining the hydrodynamic dispersion tensor as $\mathbf{D}^* = \mathbf{D}^*_M + \tilde{\mathbf{D}}$, we deduce the advection-dispersion-reaction equation as follows:

$$\frac{\partial c'}{\partial t'} + \mathbf{v}' \cdot \nabla'c' = \nabla' \cdot (\mathbf{D}^* \cdot \nabla'c') + R(c'; \mathbf{x}', t'). \tag{B2}$$

Using Eq. (1) for $\mathbf{D}^*$, upon nondimensionalizing Eq. (B2) using the scales outlined in Table I and then expressing it in spherical coordinates yields Eq. (3).

APPENDIX C: NUMERICAL SOLUTION METHODOLOGY

Equation (6) may be discretized using an implicit finite difference scheme as follows:

$$(\eta \text{Pe} v_{r(j)} + 1)T_1 + \left(\frac{2(\eta \text{Pe} v_{r(j)} + 1)}{r_{(j)}} + \eta \left. \frac{dv_r}{dr} \right|_{(j)} \right)T_2 - \text{Pe} v_{r(j)}T_3 - \left(\frac{\text{Pe}}{t - t^{\text{prev}}} + S_{P,i} \right)c_{i(j)}$$

$$= -\frac{\text{Pe} c_{i(j)}^{\text{prev}}}{t - t^{\text{prev}}} + S_{C,i}, \tag{C1}$$

$$T_1 = \frac{2(r_j - r_{j-1})c_{i(j+1)} - 2(r_{j+1} - r_{j-1})c_{i(j)} + 2(r_{j+1} - r_j)c_{i(j-1)}}{(r_{j+1} - r_j)(r_{j+1} - r_{j-1})(r_j - r_{j-1})}, \tag{C2}$$

$$T_2 = \frac{(r_j - r_{j-1})c_{i(j+1)} + (r_{j+1} + r_{j-1} - 2r_j)c_{i(j)} - (r_{j+1} - r_j)c_{i(j-1)}}{2(r_{j+1} - r_j)(r_j - r_{j-1})}, \tag{C3}$$

$$T_3 = \frac{(r_{j-1} - r_{j-2})(2r_j - r_{j-1} - r_{j-2})c_{i(j)} - (r_j - r_{j-2})^2 c_{i(j-1)} + (r_j - r_{j-1})^2 c_{i(j-2)}}{(r_{j-1} - r_{j-2})(r_j - r_{j-1})(r_j - r_{j-2})}. \tag{C4}$$

Deducing the numerical solution implies time-marching wherein Eq. (C1) is solved at each time step for each of the three species, A, B, and C, with $v_{r(j)} = 1/r_j^2$. Here $c_{i(j)}$ represents the concentration of the ith species at the jth grid node, and the superscript "prev" indicates the values from the previous time step. The terms $S_{C,i}$ and $S_{P,i}$ are the (linearized) source-term contributions corresponding to the reaction and are given by [56]: For species A, $S_{P,A} = -c_{B(j)}$, $S_{C,A} = 0$; for species B, $S_{P,B} = -c_{A(j)}$, $S_{C,B} = 0$; and for species C, $S_{P,C} = 0$, $S_{C,C} = c_{A(j)}c_{B(j)}$. At each time step, iterations are carried out until the maximum error (which is simply the square root of the average of squares of the change in values of $c_{i(j)}$ from the previous iteration) falls below the

tolerance (here taken as 10^{-5}). Last, knowing that the gradients are smoother at larger r and t, so that the system varies gradually farther from the injection point and evolves slowly at long times, the r and t grids are discretized nonuniformly, having smaller steps near $t/r = 0$ and larger steps at larger t/r.

APPENDIX D: BRIEF DERIVATION OF THE VALUE OF α APPEARING IN SECS. III B 1 AND III B 2

1. The early-time dispersion-dominated reaction-limited regime

Proceeding with Eq. (17), we emphasize that the early-time regime mandates $t \ll 1$. For this, we identify the prospective intervals for α as (1) $\alpha \leqslant 0$, (2) $0 < \alpha < \frac{1}{4}$, and (3) $\alpha \geqslant \frac{1}{4}$. These values are identified such that Eq. (17) behaves distinctly in each of the intervals, subject to the following requirements: (1) none of the terms in Eq. (17) should have a negative power of t in their prefactors; (2) the second derivative term, $d^2G_{A/B}/dz^2$, must be retained (otherwise the nature of the equation changes); and (3) when considering $\alpha < \frac{1}{4}$, the instances of the term $(zt^{\alpha - \frac{1}{4}} + 0.914\,\eta^{1/4})$ in the denominators should be rearranged to $(z + 0.914\,\eta^{1/4}t^{\frac{1}{4} - \alpha})t^{-\frac{1}{4} + \alpha}$. These requirements ensure that Eq. (17) remains physically and mathematically consistent. Provided that these requirements are fulfilled, the values of α obtained for the intervals (1) $\alpha \leqslant 0$ and (2) $0 < \alpha < \frac{1}{4}$ are, respectively, $\alpha = \frac{1}{2}$ and $\alpha = \frac{1}{4}$, both of which fall out of their designated intervals. On the other hand, for the interval (3) $\alpha \geqslant \frac{1}{4}$, we obtain $\alpha = \frac{1}{4}$, which stands out as the deduced value of α in the early time dispersion-dominated reaction-limited regime.

2. The intermediate-time dispersion-dominated mixing-limited regime

Proceeding with Eq. (24), we emphasize that the intermediate-time regime indicates $1 \ll t \ll t_{SS}$. The condition (25) then requires that the term $\eta \mathrm{Pe}\, t^{-\frac{1}{2}}(zt^{\alpha - \frac{1}{4}} + 0.914\,\eta^{1/4})^{-2}d^2G/dz^2$ must be dominant along with the reaction term, $\mathrm{Pe}\, t^{3\alpha - \frac{1}{4}}(G^2 + \mathcal{K}zG)$, simply because $t > 1$ indicates that the reaction has progressed to a significant extent. Balancing these two terms yields $\alpha = -1/12$, which is consistent with the initial assumption that $\alpha < 1/4$ as specified in Sec. III B 2. Furthermore, inserting $\alpha = -1/12$ back into Eq. (24) subject to the condition (25) indeed confirms that the rest of the terms are negligibly small as compared to the above two.

APPENDIX E: APPROXIMATE SOLUTIONS FOR THE DISPERSION-FREE SCENARIO ($\eta = 0$)

Here we present the dispersion-free counterpart (i.e. $\eta = 0$) of the analysis in Sec. III B; this has been previously reported by Comolli *et al.* [37]. For $\eta = 0$, Eq. (7) becomes

$$\mathrm{Pe}\frac{\partial \theta}{\partial t} = \frac{\partial^2 \theta}{\partial r^2} + \left(\frac{2r - \mathrm{Pe}}{r^2}\right)\frac{\partial \theta}{\partial r}. \tag{E1}$$

Furthermore, following a path similar to that in Sec. III B 1, at early times, the reaction front is sufficiently close to the injection point ($r_f \ll 1$) and occupies a sufficiently small region for the following assumption to hold within the reaction zone: $|\partial^2\theta/\partial r^2| \ll |[(2r - \mathrm{Pe})/r^2]\partial\theta/\partial r|$. As a consequence, keeping only the leading terms, Eq. (E1) simplifies to $\theta_t = r^{-1}\theta_r$, which admits a similarity solution, with the similarity variable $\hat{\xi} = r^3/3t$; this leads to the ODE, $d\theta/d\hat{\xi} = 0$. The solution to this ODE will be $\theta = \Theta_0$ (a constant). Note, however, that the above simplification reduces the order of the original equation [Eq. (E1)], thus indicating the presence of an internal boundary layer [57], which essentially encompasses the reaction front. The simplified ODE on the other hand governs θ in the outer regions on either side of the front, hence the constant $\Theta_0 = \pm 1$, depending on which side of the front is being considered. Within the internal boundary layer (i.e., the front) θ varies rapidly between 1 and -1. Because our aim is simply to deduce the location of the front (defined as the location where $\theta = 0$), we note that it must be located at $\hat{\xi} = \xi_0$ (a constant),

giving us the expression for $r_f(t)$ as (without commenting on the value of ξ_0 explicitly),

$$r_f = 3\xi_0 t^{\frac{1}{3}} = \Xi t^{\frac{1}{3}} \sim t^{\frac{1}{3}}. \tag{E2}$$

In fact, with the reaction being negligible at early times, the front is simply advected by the solvent fluid such that the front position follows:

$$r_f = (3t)^{\frac{1}{3}}. \tag{E3}$$

Further, we again assume that $c_{A/B}$ have forms similar to those in Eq. (16), with which Eq. (6) for $c_{A/B}$ in the vicinity of the reaction front transforms to

$$\frac{d^2 G_{A/B}}{dz^2} + \left[\frac{t^{\alpha - \frac{1}{3}}}{\left(zt^{\alpha - \frac{1}{3}} + \Xi\right)} - \frac{\mathrm{Pe}\, t^{\alpha - \frac{2}{3}}}{\left(zt^{\alpha - \frac{1}{3}} + \Xi\right)^2} + \alpha \mathrm{Pe}\, zt^{2\alpha - 1} \right] \frac{dG_{A/B}}{dz} - \mathrm{Pe}\, t^{2\alpha} c_A c_B = 0. \tag{E4}$$

Following Comolli *et al.* [37], $\alpha = 1/2$, and subsequently Eq. (E4) simplifies to, $G''_{A/B} + (z\mathrm{Pe}/2)G'_{A/B} = 0$. The exact analytical solution of this equation is $c_{A/B} = 1/2 \mp (1/2)\mathrm{erf}(\sqrt{\mathrm{Pe}}z/2)$, where the "−" sign is for A and the "+" sign for B. Substituting the expression for r in terms of z and the above expressions for c_A and c_B into Eq. (9), we deduce

$$\bar{R} \sim t^{\frac{7}{6}}, \tag{E5}$$

which gives us [using Eq. (11)] for the product mass

$$M_C \sim t^{\frac{13}{6}}. \tag{E6}$$

On the other hand, using Eq. (8), the width may be estimated as

$$w_f \sim t^{\alpha} = t^{1/2}. \tag{E7}$$

APPENDIX F: ALTERNATIVE DERIVATION OF THE SCALING ESTIMATES FOR THE STEADY-STATE GLOBAL REACTION RATE ($\bar{R}_{(S)}$)

The global reaction rate may also be estimated by considering Eq. (6) for the species B, which may be multiplied by $4\pi r^2$ and integrated over the entire domain to arrive at the following:

$$4\pi \int_0^\infty (\eta \mathrm{Pe} + r^2) \frac{d^2 c_B}{dr^2}\, dr + 4\pi \int_0^\infty (2r - \mathrm{Pe}) \frac{dc_B}{dr}\, dr - 4\pi \mathrm{Pe} \int_0^\infty |R_B| r^2\, dr \approx 0, \tag{F1}$$

where $|R_B| = c_A c_B$; see Eq. (3b). We identify the last integral on the left-hand side as the steady global reaction rate ($\bar{R}_{(S)}$). Furthermore, since the reaction between A and B (and hence their variations) is mostly confined to a region close to the front and considering that in the steady state the front is sufficiently far ahead from the injection point for its radial position to far exceed its width ($r_{f(S)} \gg w_{f(S)}$), we may approximate $r \approx r_{f(S)}$ in the first two integrals in Eq. (F1). This yields for the global reaction rate (subjected to the boundary conditions for c_B)

$$\bar{R}_{(S)} = 4\pi \int_0^\infty |R_B| r^2\, dr \approx \frac{4\pi(2r_{f(S)} - \mathrm{Pe})}{\mathrm{Pe}}. \tag{F2}$$

In the weak dispersion scenario ($\eta \ll \mathrm{Pe}$), $r_{f(S)} \sim \mathrm{Pe}$ [see Eq. (42)], and this leads to $\bar{R}_{(S)} \sim \mathrm{Pe}^0$. On the other hand, for strong dispersion ($\eta \gg \mathrm{Pe}$), $r_{f(S)} \sim \sqrt{\eta \mathrm{Pe}}$ [see Eq. (44)], which results in $\bar{R}_{(S)} \sim \sqrt{\eta/\mathrm{Pe}}$. However, the prefactors of these scaling estimates are better approximated by the analysis of Sec. III B 3.
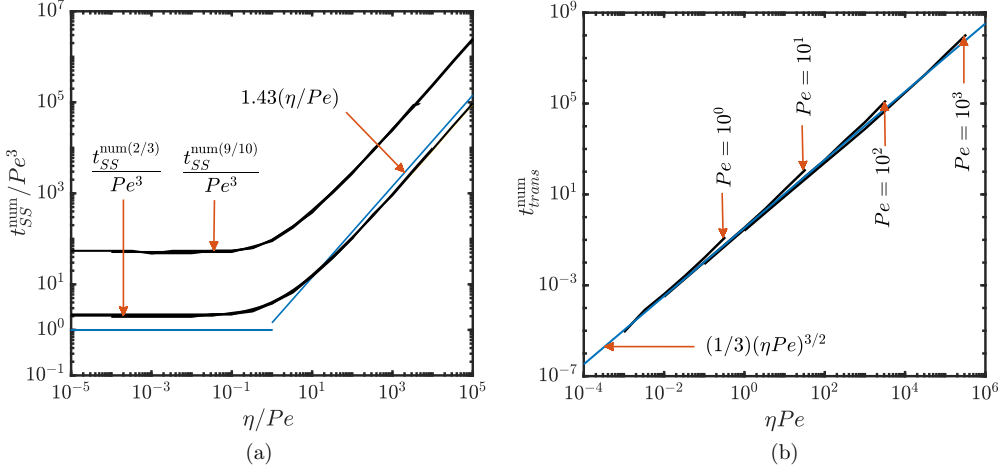
FIG. 8. Variations in the numerically computed (a) steady-state time normalized by Pe^3 (i.e., t_{SS}/Pe^3) and (b) transition time t_{trans}, with η/Pe; the expected scaling patterns of these transition times with η/Pe as per Sec. III B 4 are also plotted as the labeled floating blue lines.

APPENDIX G: ALTERNATIVE DERIVATION OF THE TRANSITION TIME TO STEADY STATE (t_{SS})

An alternative approach to derive the steady-state time is to consider the period when the front is approaching the stationary state, such that $x = r - r_{f(S)} \ll r_{f(S)}$. Then we may define $\theta = \hat{\theta} + \theta_{(S)}$ and approximate r with $r_{f(S)}$ in Eq. (7), which simplifies to

$$\mathrm{Pe}\frac{\partial\hat{\theta}}{\partial t} = \left(\frac{\eta\mathrm{Pe}}{r_{f(S)}^2} + 1\right)\frac{\partial^2\hat{\theta}}{\partial x^2} + \left(\frac{2r_{f(S)} - \mathrm{Pe}}{r_{f(S)}^2}\right)\frac{\partial\hat{\theta}}{\partial x}. \tag{G1}$$

Here $\hat{\theta}$ represents the unsteady part of θ; it must decay to zero as the steady state is approached. Using separation of variables, and with the condition that at sufficiently large times, $\hat{\theta} = 0$ at $x = 0$, Eq. (G1) can be solved to

$$\hat{\theta} = C_0 e^{-\lambda t}\left[e^{-\frac{x}{2r_{f(S)}}(1 - \sqrt{1 - 2\mathrm{Pe}\lambda r_{f(S)}^2})} - e^{-\frac{x}{2r_{f(S)}}(1 + \sqrt{1 - 2\mathrm{Pe}\lambda r_{f(S)}^2})}\right]. \tag{G2}$$

Evidently λ^{-1} (inverse of the separation constant) represents the timescale of decay for $\hat{\theta}$ and is therefore a good approximation for t_{SS}. To obtain an estimate for λ, we use the condition that as $x \to -r_{f(S)}$ (i.e., as we approach the injection point), $\hat{\theta} \to 0$. Imposing this condition yields as a leading approximation, $\lambda^{-1} \sim \mathrm{Pe}\, r_{f(S)}^2$, which will translate into the same scalings as presented in Eq. (46), when Eqs. (42) and (44) are, respectively, substituted for $r_{f(S)}$.

APPENDIX H: VARIATIONS IN THE TRANSITION TIMES (t_{SS} AND t_{trans}) WITH Pe

Figure 8 presents the variations (numerically computed) in the steady-state transition time normalized by Pe^3 (i.e., t_{SS}/Pe^3) [in Fig. 8(a)] and the transition time between the dispersion and the diffusion-dominated regimes [t_{trans}, in Fig. 8(b)] as functions of η/Pe. Their expected analytical approximations from Eqs. (46) and (48) are also shown in the two panels; they exhibit very good agreement with the numerical estimates. Indeed, t_{SS}/Pe^3 is independent of η/Pe [Fig. 8(a)] in the weak-dispersion regime ($\eta/\mathrm{Pe} \ll 1$), and it scales as η/Pe in the strong-dispersion scenario ($\eta/\mathrm{Pe} \gg 1$), as predicted by Eq. (46). On the other hand, t_{trans} is approximated consistently by $(1/3)(\eta\mathrm{Pe})^{\frac{3}{2}}$ [Fig. 8(b)], as expected from Eq. (48).

[1] M. Dentz, T. Le Borgne, A. Englert, and B. Bijeljic, Mixing, spreading and reaction in heterogeneous media: A brief review, J. Contam. Hydrol. **120–121**, 1 (2011).

[2] M. Rolle and T. Le Borgne, Mixing and reactive fronts in the subsurface, Rev. Mineral. Geochem. **85**, 111 (2019).

[3] A. J. Valocchi, D. Bolster, and C. J. Werth, Mixing-limited reactions in porous media, Transp. Porous Media **130**, 157 (2019).

[4] P. K. Kitanidis and P. L. McCarty, *Delivery and Mixing in the Subsurface: Processes and Design Principles for in Situ Remediation*, SERDP ESTCP Environmental Remediation Technology (SERDP/ESTCP, Vol. 4) (Springer Science & Business Media, New York, 2012).

[5] A. Faisal, A. Sulaymon, and Q. Khaliefa, A review of permeable reactive barrier as passive sustainable technology for groundwater remediation, Int. J. Environ. Sci. Technol. **15**, 1123 (2018).

[6] S. Mohammadian, B. Krok, A. Fritzsche, C. Bianco, T. Tosco, E. Cagigal, B. Mata, V. Gonzalez, M. Diez-Ortiz, V. Ramos *et al.*, Field-scale demonstration of *in situ* immobilization of heavy metals by injecting iron oxide nanoparticle adsorption barriers in groundwater, J. Contam. Hydrol. **237**, 103741 (2021).

[7] M. L. Szulczewski, C. W. MacMinn, H. J. Herzog, and R. Juanes, Lifetime of carbon capture and storage as a climate-change mitigation technology, Proc. Natl. Acad. Sci. USA **109**, 5185 (2012).

[8] K. Gautam and P. Narayana, On the stability of carbon sequestration in an anisotropic horizontal porous layer with a first-order chemical reaction, Proc. R. Soc. A **475**, 20180365 (2019).

[9] R. Tarkowski, Underground hydrogen storage: Characteristics and prospects, Renew. Sustain. Energy Rev. **105**, 86 (2019).

[10] M. Lysyy, G. Ersland, and M. Fernø, Pore-scale dynamics for underground porous media hydrogen storage, Adv. Water Resour. **163**, 104167 (2022).

[11] L. Burté, C. A. Cravotta III, L. Bethencourt, J. Farasin, M. Pédrot, A. Dufresne, M.-F. Gérard, C. Baranger, T. Le Borgne, and L. Aquilina, Kinetic study on clogging of a geothermal pumping well triggered by mixing-induced biogeochemical reactions, Environ. Sci. Technol. **53**, 5848 (2019).

[12] O. Bochet, L. Bethencourt, A. Dufresne, J. Farasin, M. Pédrot, T. Labasque, E. Chatton, N. Lavenant, C. Petton, B. W. Abbott *et al.*, Iron-oxidizer hotspots formed by intermittent oxic–anoxic fluid mixing in fractured rocks, Nat. Geosci. **13**, 149 (2020).

[13] J. Priyadarshani, P. Awasthi, P. Karan, S. Das, and S. Chakraborty, Transport of vascular endothelial growth factor dictates on-chip angiogenesis in tumor microenvironment, Phys. Fluids **33**, 031910 (2021).

[14] P. de Anna, M. Dentz, A. Tartakovsky, and T. Le Borgne, The filamentary structure of mixing fronts and its control on reaction kinetics in porous media flows, Geophys. Res. Lett. **41**, 4586 (2014).

[15] P. de Anna, J. Jimenez-Martinez, H. Tabuteau, R. Turuban, T. Le Borgne, M. Derrien, and Y. Méheust, Mixing and reaction kinetics in porous media: An experimental pore scale quantification, Environ. Sci. Technol. **48**, 508 (2014).

[16] T. D. Nevins and D. H. Kelley, Optimal Stretching in Advection-Reaction-Diffusion Systems, Phys. Rev. Lett. **117**, 164502 (2016).

[17] Y. Ye, G. Chiogna, C. Lu, and M. Rolle, Plume deformation, mixing and reaction kinetics in 3-d heterogeneous anisotropic porous media, in *InterPore2020: 12th Annual Meeting & Short Courses* (InterPore-International Society for Porous Media, 2020), pp. 341–342.

[18] Y. Ye, G. Chiogna, C. Lu, and M. Rolle, Plume deformation, mixing, and reaction kinetics: An analysis of interacting helical flows in three-dimensional porous media, Phys. Rev. E **102**, 013110 (2020).

[19] S. Sen, P. Singh, J. Heyman, T. Le Borgne, and A. Bandopadhyay, The impact of stretching-enhanced mixing and coalescence on reactivity in mixing-limited reactive flows, Phys. Fluids **32**, 106602 (2020).

[20] F. Ziliotto, M. Basilio Hazas, M. Rolle, and G. Chiogna, Mixing enhancement mechanisms in aquifers affected by hydropeaking: Insights from flow-through laboratory experiments, Geophys. Res. Lett. **48**, e2021GL095336 (2021).

[21] A. Comolli, A. De Wit, and F. Brau, Dynamics of $A + B \rightarrow c$ reaction fronts under radial advection in a Poiseuille flow, Phys. Rev. E **104**, 044206 (2021).

[22] M. Basilio Hazas, F. Ziliotto, M. Rolle, and G. Chiogna, Linking mixing and flow topology in porous media: An experimental proof, Phys. Rev. E **105**, 035105 (2022).

[23] P. Meunier and E. Villermaux, The diffuselet concept for scalar mixing, J. Fluid Mech. **951**, A33 (2022).

[24] S. H. Lee and P. K. Kang, Three-Dimensional Vortex-Induced Reaction Hot Spots at Flow Intersections, Phys. Rev. Lett. **124**, 144501 (2020).

[25] A. Bandopadhyay, T. Le Borgne, Y. Méheust, and M. Dentz, Enhanced reaction kinetics and reactive mixing scale dynamics in mixing fronts under shear flow for arbitrary Damköhler numbers, Adv. Water Resour. **100**, 78 (2017).

[26] T. L. Borgne, T. R. Ginn, and M. Dentz, Impact of fluid deformation on mixing-induced chemical reactions in heterogeneous flows, Geophys. Res. Lett. **41**, 7898 (2014).

[27] F. Brau, G. Schuszter, and A. De Wit, Flow Control of $A + B \rightarrow C$ Fronts by Radial Injection, Phys. Rev. Lett. **118**, 134101 (2017).

[28] F. Brau and A. De Wit, Influence of rectilinear vs radial advection on the yield of $A + B \rightarrow C$ reaction fronts: A comparison, J. Chem. Phys. **152**, 054716 (2020).

[29] E. Guilbert, C. Almarcha, and E. Villermaux, Chemical reaction for mixing studies, Phys. Rev. Fluids **6**, 114501 (2021).

[30] E. Guilbert and E. Villermaux, Chemical reactions rectify mixtures composition, Phys. Rev. Fluids **6**, L112501 (2021).

[31] E. Guilbert, B. Metzger, and E. Villermaux, Chemical production on a deforming substrate, J. Fluid Mech. **934**, R1 (2022).

[32] L. Gálfi and Z. Rácz, Properties of the reaction front in an $A + B \rightarrow C$ type reaction-diffusion process, Phys. Rev. A **38**, 3151 (1988).

[33] H. Larralde, M. Araujo, S. Havlin, and H. E. Stanley, Reaction front for $A + B \rightarrow C$ diffusion-reaction systems with initially separated reactants, Phys. Rev. A **46**, 855 (1992).

[34] A. De Wit, Chemo-hydrodynamic patterns and instabilities, Annu. Rev. Fluid Mech. **52**, 531 (2020).

[35] A. Bandopadhyay, Y. Méheust, and T. Le Borgne, Reaction front dynamics under shear flow for arbitrary Damköhler numbers, in *EGU General Assembly Conference Abstracts* (EGU, Vienna, Austria, 2016), pp. EPSC2016–16167.

[36] U. Ghosh, T. Borgne, D. Jougnot, N. Linde, and Y. Méheust, Geoelectrical signatures of reactive mixing: A theoretical assessment, Geophys. Res. Lett. **45**, 3489 (2018).

[37] A. Comolli, A. De Wit, and F. Brau, Dynamics of $A + B \rightarrow C$ reaction fronts under radial advection in three dimensions, Phys. Rev. E **100**, 052213 (2019).

[38] J. Bear, *Modeling Phenomena of Flow and Transport in Porous Media*, Theory and Applications of Transport in Porous Media (TATP, Vol. 31) (Springer, Cham, Switzerland, 2018).

[39] L. de Arcangelis, J. Koplik, S. Redner, and D. Wilkinson, Hydrodynamic Dispersion in Network Models of Porous Media, Phys. Rev. Lett. **57**, 996 (1986).

[40] G. Dagan, Perturbation solutions of the dispersion equation in porous mediums, Water Resour. Res. **7**, 135 (1971).

[41] P. Saffman, A theory of dispersion in a porous medium, J. Fluid Mech. **6**, 321 (1959).

[42] R. Zhou, H. Zhan, and K. Chen, Reactive solute transport in a filled single fracture-matrix system under unilateral and radial flows, Adv. Water Resour. **104**, 183 (2017).

[43] R. M. Neupauer, L. J. Sather, D. C. Mays, J. P. Crimaldi, and E. J. Roth, Contributions of pore-scale mixing and mechanical dispersion to reaction during active spreading by radial groundwater flow, Water Resour. Res. **56**, e2019WR026276 (2020).

[44] T. Le Borgne, M. Dentz, and E. Villermaux, Stretching, Coalescence, and Mixing in Porous Media, Phys. Rev. Lett. **110**, 204501 (2013).

[45] T. Le Borgne, M. Dentz, and E. Villermaux, The lamellar description of mixing in porous media, J. Fluid Mech. **770**, 458 (2015).

[46] H. A. Stone and H. Brenner, Dispersion in flows with streamwise variations of mean velocity: Radial flow, Ind. Eng. Chem. Res. **38**, 851 (1999).

[47] B. Noetinger, D. Roubinet, A. Russian, T. Le Borgne, F. Delay, M. Dentz, J.-R. De Dreuzy, and P. Gouze, Random walk methods for modeling hydrodynamic transport in porous and fractured media from pore to reservoir scale, Transp. Porous Media **115**, 345 (2016).

[48] F. W. Olver, D. W. Lozier, R. F. Boisvert, and C. W. Clark, *NIST Handbook of Mathematical Functions Hardback and CD-ROM* (Cambridge University Press, New York, 2010).

[49] J. Bear and A. Verruijt, *Modeling Groundwater Flow and Pollution*, Theory and Applications of Transport in Porous Media (D. Reidel Publishing Company, Dordrecht, 1987).

[50] D. Harleman and R. Rumer, Longitudinal and lateral dispersion in an isotropic porous medium, J. Fluid Mech. **16**, 385 (1963).

[51] T. Miyauchi and T. Kikuchi, Axial dispersion in packed beds, Chem. Eng. Sci. **30**, 343 (1975).

[52] M. Xu and Y. Eckstein, Statistical analysis of the relationships between dispersivity and other physical properties of porous media, Hydrogeology J. **5**, 4 (1997).

[53] J. G. de Carvalho and J. Delgado, Overall map and correlation of dispersion data for flow through granular packed beds, Chem. Eng. Sci. **60**, 365 (2005).

[54] J. Delgado, Longitudinal and transverse dispersion in porous media, Chem. Eng. Res. Des. **85**, 1245 (2007).

[55] A. E. Scheidegger, General theory of dispersion in porous media, J. Geophys. Res. **66**, 3273 (1961).

[56] S. V. Patankar, *Numerical Heat Transfer and Fluid Flow* (Hemisphere Publishing Corporation, New York, 1980).

[57] C. M. Bender and S. A. Orszag, *Advanced Mathematical Methods for Scientists and Engineers I: Asymptotic Methods and Perturbation Theory* (Springer Science & Business Media, New York, 1999).